VRIJE UNIVERSITEIT

MASTER THESIS

Multi-Energy Deconvolution Scanning Electron Microscopy

The 3D Imaging of Nanostructures using Backscattered Electrons

Author:
Michiel de Goede

Supervisor:
dr. Erik C. Garnett
Examiner:
Prof. dr. Albert Polman
Examiner:
Prof. dr. Rinke J. Wijngaarden

Master Thesis Physics
Advanced Matter and Energy Physics Track
FOM Institute AMOLF
Nanoscale Solar Cells Group
January–December 2014
60 ECTS

Acknowledgements

Abstract

The aim of nanotechnology is to understand the properties of structures at the smallest length scales. One of the most fundamental properties of any nanostructure is its three-dimensional composition. Current state-of-the-art methods for such characterization which allow for not only surface topography but also internal structure mapping are TEM tomography and FIBSEM cross-sectional milling. Multi-Energy Deconvolution Scanning Electron Microscopy (MEDSEM) is a novel alternative to these electron microscope tomography techniques. MEDSEM works by obtaining backscattered electron images at multiple electron acceleration voltages and subsequently applying a deconvolution to the obtained image stack. Since every backscattered electron image contains some mixture of information from the structure's interior, and the penetration depth of electrons is larger at increased beam acceleration voltages, depth-information can already be retrieved by only varying the beam acceleration voltage. Furthermore, imaging backscattered electron provides elemental contrast as a function of depth. In this study we show that this approach allows the probing of the interior up to depths of $\sim 100\pm10$ nm for both Ag@Cu$_2$O and Au@Cu$_2$O core-shell nanowires and the visualization of Au@Cu$_2$O core-shell nanoparticles lying underneath material layers with a thickness of up to 105 ± 10 nm. This is achieved at nanometer length scales by a simple, non-destructive alternative to conventional electron microscope tomography.

Contents

Chapter 1

Introduction

1.1 Volumetric Electron Microscopy

A microscope is a device that allows the visualization of systems that cannot be observed by the naked eye. Modern optical microscopes not only optically magnify small systems, they can also image a system's interior by optical sectioning methods. For instance, M.B. Ahrens et al. (2013) used this method to record *in vivo* the activity throughout the entire volume of the brain of the larval zebrafish[1]. However, imaging the interior of smaller systems requires the Scanning Electron Microscope (SEM).

The SEM uses electrons instead of photons to form images. Since the wavelength of an electron is much smaller than the diffraction limit in optical microscopy, ultra-high resolutions down to 50 pm can be reached, as demonstrated by R. Erni et al. (2009) in a transmission electron microscope (TEM)[2]. The SEM forms an image by scanning a primary electron beam over a surface while collecting signals emitted from the sample, as illustrated in Figure 1.1.

The SEM can also be used to image three-dimensional (3D) systems. One method therefore is 'slice-and-view'. Slice-and-view can be interpreted literally: one repeatedly images an interface and subsequently removes a layer of material while destroying the sample in the process. This method is used in both Serial Block-Face Scanning Electron Microscopy (SBFSEM) and Focused Ion Beam Scanning Electron Microscopy (FIBSEM). In SBFSEM, a diamond knife repeatedly removes thin slices of the top of the sample while imaging the exposed block-face[3]. In this way, for instance, Thompson et al. (2013) succeeded in mapping the elemental distribution of aluminum alloys at a slice thickness of 15 nm[4], as shown in Figure 1.2 A. On the other hand, FIBSEM uses a beam of gallium ions for the cross-sectional milling of thin
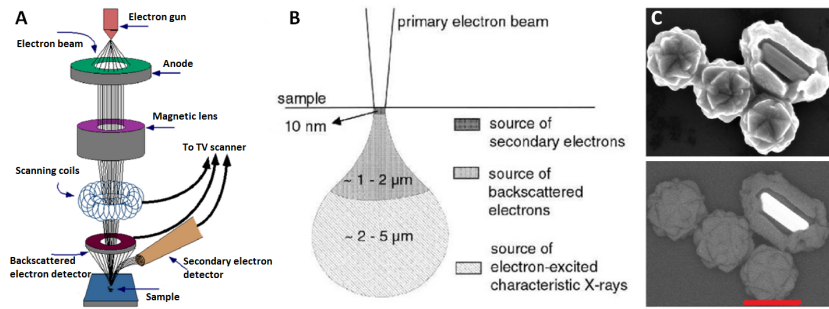
Figure 1.1: *Working principles of the SEM.* ***A,*** *Schematic of electron microscope. Image obtained from [7].* ***B,*** *Interaction volume of the beam indicating the several regions from which characteristic signals originate. Image obtained from [7].* ***C,*** *Top: secondary electron image showing surface topography. Bottom: backscattered electron image showing elemental contrast between Cu_2O (gray) and Au region (white). The scale bar is 400 nm.*

layers from the sample. By using FIBSEM Wei et al. (2012) imaged a whole yeast cell in 3D [5], as shown in Figure 1.2 B. Slice-and-view allows voxel sizes down to $3 \times 3 \times 3\,\text{nm}^3$[6].

The 3D imaging of even smaller systems can be achieved by TEM Tomography (TEMT). With TEMT one acquires a 'tilt-series' of transmission electron images by imaging the sample at various tilt angles. Then, a 3D reconstruction of the sample is calculated by a backprojection algorithm from the absorption contrast on the acquired tilt-series. In this way van Aert et al. succeeded in fully mapping the positions of 784 atoms in an Ag nanocluster[8]. Furthermore, Haberfehlner et al. (2013) used TEMT to reveal the 3D chemical structure of a tri-gate transistor for microelectronic inspection[9]. Both examples were obtained at sub-nanometer sized voxels and are shown respectively in Figures 1.2 C and D.

These three methods can not only image but also perform chemical characterization in 3D at nanometer length scales. This can be achieved by either detecting elemental contrast on backscattered electron (BSE) or transmission electron images or by employing energy-dispersive X-ray spectroscopy. The possibility of detecting the 3D composition of nanostructures is what makes TEMT, SBFSEM and FIBSEM frequently applied characterization methods in materials science, nanotechnology and the life sciences.
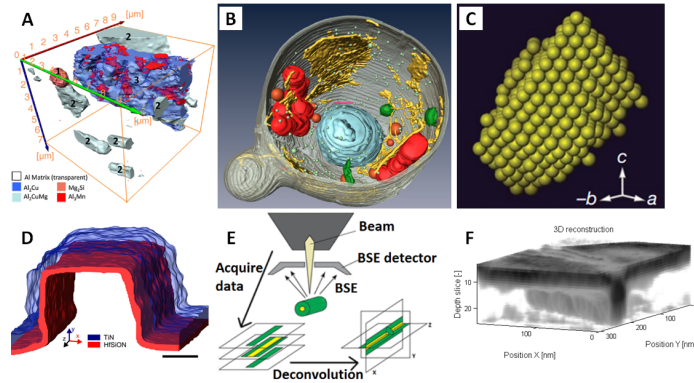
Figure 1.2: *Volumetric electron microscopy.* **A,** *3D elemental map of an Al-Cu alloy. Image obtained from [4].* **B,** *3D image of a yeast cell containing various cell components. Image obtained from [5].* **C,** *3D representation of Ag atoms in a nanocluster. Image obtained from [8].* **D,** *Tri-gate transistor in 3D. The scale bar is 10 nm. Image obtained from [9].* **E,** *The workflow of MEDSEM.* **F,** *3D image obtained with MEDSEM of an Au nanowire lying underneath an Au sheet.*

1.2 Multi-Energy Deconvolution Scanning Electron Microscopy

Despite the resolving power in 3D of electron microscopes, serious drawbacks exist for them. Both SBFSEM and FIBSEM irreparably destroy the sample while acquiring a 3D image and thus seriously restrict the characterization workflow. Furthermore, their data throughput can be low when cutting many, thin slices[6]. On the other hand, TEMT requires relatively thin and specially prepared samples that do not allow a wide viewing field [10]. In addition, acquiring a tilt-series over a large range of angles requires a long total beam exposure time at relatively high beam energies and thus possibly damages the sample. Finally, all three devices are complex and expensive. These drawbacks can be overcome by Multi-Energy Deconvolution Scanning Electron Microscopy (MEDSEM), a novel 3D SEM characterization tool that could serve as an alternative, or addition, to SBFSEM, FIBSEM and TEMT.

MEDSEM was recently developed by FEI Company to image biological structures in 3D[11]. It works by solving the inverse problem of BSE image formation in an electron microscope[12–14]. A BSE image is formed from the convolution of the primary beam with a sample's 3D structure. Increasing the acceleration voltage V_{acc} allows the BSEs to probe deeper regions in the sample prior to detection and the deconvolution then encompasses deeper regions

3

of the structure. Then, acquiring BSE images at various V_{acc}'s, a multi-energy BSE image stack, and the deconvolution thereof provides a representation of the 3D structure of the sample. However, performing the deconvolution is far from trivial and to approximately solve it a linearized blind deconvolution, or Blind Source Separation (BSS), is applied. While doing so, both a point-spread-function (PSF) of the beam broadening along depth and a layered 3D structure of the sample are simultaneously estimated without a priori information of both. This is done by applying similar BSS methods as encountered in problems of speech recognition[15], medical imaging[16], astronomy[17], fluorescence microscopy[18] and geology[19]. Then, a 3D image of the sample can be reconstructed, as shown in Figures 1.2 E and F. However, the depth resolution and probing depth are limited compared to the conventional 3D electron microscope methods.

Despite these limitations, MEDSEM also offers advantages over conventional electron microscope tomography. For instance, besides sample thickness almost no sample restrictions exist. Furthermore, the 3D imaging is non-destructive and large field widths at high throughput can be imaged. Finally, it requires only an electron beam and a backscattered electron detector. This makes MEDSEM easy to use and highly accessible for the nanotechnology community, since most nanoscience groups already use SEM extensively for the characterization of nanostructures.

Until now, MEDSEM has been developed within FEI research for the imaging of stained biological tissues in 3D. These samples exhibit high elemental contrast between the epoxy matrix and osmium staining. Furthermore, low beam energies already allow deep penetration of the BSE's into the sample due to the low stopping power thereof. However, dense samples with lower elemental contrast do not have these features and it is not yet known how the acquisition and deconvolution of multi-energy BSE images can reconstruct the 3D structure of such samples. In general, 3D imaging of nanostructures with MEDSEM has not been explored yet.

The purpose of the research study presented in this thesis is to investigate the feasibility of applying MEDSEM to the 3D characterization of Ag@Cu$_2$O and Au@Cu$_2$O core-shell nanostructures. More specifically, the depth information present on multi-energy BSE images of nanostructures, their deconvolution to reconstruct a nanostructure in 3D, the quality thereof, till what depths structural features can still be retrieved, the corresponding depth resolutions and artifacts limitating the 3D imaging of MEDSEM are studied.

Chapter 2

Principles of MEDSEM

2.1 Electron Trajectories in Solids

Electrons are spin $1/2$ particles that carry a negative elementary charge $q_e = 1.602 \times 10^{-19}$ C. They can interact in multiple ways with their environment through their spin and charge. In the SEM, Coulomb scattering from atoms is the most important interaction that contributes to the formation of BSE images.

Elastic Coulomb scattering is the process in which an electron's trajectory is deflected without energy loss upon colliding with the nucleus of an atom of charge Zq_e, where Z is its atomic number. This is described by the differential scattering cross section $d\sigma/d\Omega$, which is the ratio of electrons scattered from the cross-section σ into the unit solid angle $d\Omega$ to the incident electron flux. For spinless electrons that neither penetrate the nucleus nor scatter from other electrons, $d\sigma/d\Omega$ is given by Rutherford's scattering formula[20–22]:

$$d\sigma/d\Omega = \left[\frac{Zq_e^2}{4\pi\epsilon_0 E}\right]^2 \frac{1}{\sin^4(\theta/2)} \qquad (2.1)$$

where E is the energy of the incident electron, ϵ_0 is the permittivity of the vacuum and θ is the scattering angle. Equation 2.1 does not hold any more for energies $E \leqslant 10$ keV and the more accurate and general Mott scattering theory must be applied, resulting in a correction factor to Equation 2.1 [23–25].

An electron also loses energy through inelastic scattering events as it moves through a solid. A common energy-loss mechanism is secondary electron emission. Secondary electrons are ionized inner-shell electrons ejected from their parent atom. Subsequently, an electron from one of the outer shells can fill up the inner-shell hole while emitting an X-ray or another outer-shell
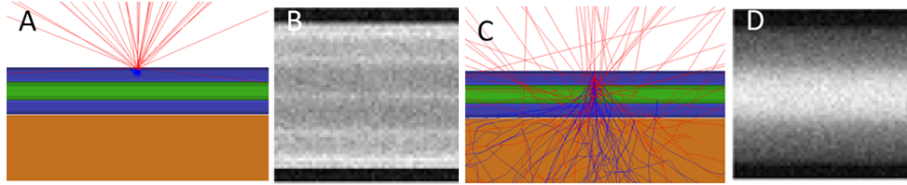
Figure 2.1: *The MC calculations of BSE trajectories (red) in an Au@Cu$_2$O core shell nanowire with the Au core in green and the Cu$_2$O shell in blue on an orange silicon substrate. Outer radius of the nanowire is 84 nm.* **A,** *Wire cross section containing electron trajectories at V_{acc} =1 kV.* **B,** *BSE image of the nanowire at V_{acc} =1 kV.* **C,** *Wire cross section containing electron trajectories at V_{acc} =10 kV.* **D,** *BSE image of the nanowire at V_{acc} =10 kV.*

electron.

Electron energy loss is not described by discrete energy-loss steps, but by a continuous energy loss model. In this model the rate dE/dS (keV/cm) of energy loss per travelled distance S is given by the modified Bethe Equation [26, 27]:

$$\frac{dE}{dS} = -78500\frac{\rho Z}{AE} \log\left(\frac{1.166E}{J}\right) \qquad (2.2)$$

where ρ is the density of the material, Z the average atomic number, A the average atomic weight and J the mean ionization potential, which is the average rate of energy transfer due to all possible inelastic events [27, 28].

An electron's trajectory through a solid is determined by Equations 2.1 (or Mott theory) and 2.2. Despite this calculation being analytically impossible to solve, good estimates thereof can be obtained by performing Monte Carlo (MC) electron ray tracing calculations[22, 29–32]. In these, the primary beam electrons strike a randomly sampled point within the beam spot on the sample. Then, the distance L an electron travels until a collision event occurs is randomly sampled. Its new energy after traveling a distance L is then calculated by $E_{\text{at collision}} = E_{\text{before collision}} + \frac{dE}{dS}L$. Finally, the deflection angle is randomly sampled from either the Rutherford or Mott scattering $d\sigma/d\Omega$. The last three steps are repeated until an electron exits the sample in the direction of the incoming beam, which is then called a BSE.

Tracing many BSE trajectories obtained from MC calculations provides insight in how they form BSE images. By collecting the BSEs while moving the beam spot over the sample, a BSE image can be simulated, as shown in Figure 2.1. All MC calculations in this study are performed with the Casino v3.2 MC software[32].

2.2 Image Formation in MEDSEM

The backscatter coefficient is the fraction of BSEs to primary beam electrons. A BSE image contains a representation of the spatially varying backscatter coefficient of the sample. For $V_{acc} \leqslant 100$ kV the backscatter coefficient of bulk materials is almost independent of V_{acc}[33]. However, the interaction volume's size and shape is highly dependent on V_{acc}, as can be seen in Figures 2.1 A and C. Therefore, at high V_{acc} a BSE image is formed from BSEs that probed deeper subsurface regions.

This mixture of BSEs emerging from several sample regions while forming a BSE image $Y_{V_{acc}}$ at some V_{acc} is described by a convolution between the primary beam and the sample's 3D structure:

$$Y_{V_{acc}}(x, y) = H_{V_{acc}}(x, y, z) * O(x, y, z) \tag{2.3}$$

where $H_{V_{acc}}(x, y, z)$ is the corresponding beam broadening PSF and $O(x, y, z)$ the 3D structure of the sample[12–14].

In principle, the image formation is similar to the optical sectioning method where one images at several focal planes within the sample. There, the image at a certain depth is blurred by the optical PSF[1]. A BSE image is formed similarly, since at a V_{acc} a focal plane at a certain depth within the sample is imaged[34–36]. However, now the BSE image is blurred in the sense that it also contains a signal arising from planes above and below its focal plane[36].

This idea is illustrated in Figure 2.2, which shows how a BSE image contains depth information of a structure. Figure 2.2 A shows the distribution of maximum depth that electrons penetrate in Au before emerging as a BSE for several V_{acc}, as obtained from MC calculations. There, the vertical lines indicate the maximum depth that occurs with highest frequency. Figure 2.2 B shows how this depth distribution of BSEs results in blurred image formation. The BSE image Y_1 at low V_{acc} contains mostly the signal of material layer O_1, since this is where the interaction volume is mostly orientated. Thus, one can say that image Y_1 represent the top structure of the sample. Upon increasing V_{acc} BSE image Y_2 contains a mixture of the signal from both layers O_1 and O_2 and, therefore, represents a mixture of the structures of these. Further increasing V_{acc} gives an mixture of all layers and the particle hidden in layer O_3 can be imaged, as depicted on the BSE images Y_3 and Y_4.

As already suggested by Figure 2.2, some simplifications can be applied to approximately describe the image formation of Equation 2.3. One way is to assume that the image formation follows an *instantaneous mixing* model. In this model the sample is treated as consisting out of n two-dimensional virtual layers O_i containing the structural information of the sample, which could be
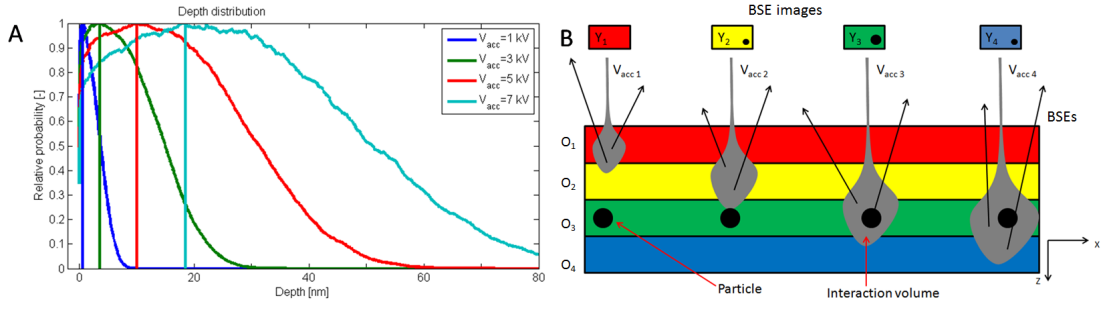
Figure 2.2: *BSE image formation.* ***A,*** *MC calculations of maximum penetration depth in Au of BSEs.* ***B,*** *Cartoon of imaging a buried particle at various* V_{acc}.

imaged if the other layers where absent. Furthermore, it is assumed that the image formation is linearized, meaning that a BSE image $Y_{V_{acc}}(x, y)$ contains a weighted linear mixture of all these layers O_i's and that the convolution is limited to a blurring in the Z-direction. In this way the virtual layers are the deconvolved BSE images whose linear superposition forms the acquired multi-energy BSE images. The image formation can then be described by:

$$Y_{V_{acc}}(x, y) = h_{1,V_{acc}} O_1 + h_{2,V_{acc}} O_2 + \cdots + h_{n,V_{acc}} O_n \qquad (2.4)$$

where $h_{i,V_{acc}}$ are the mixing weight factors[12–14, 36]. By taking n BSE images at various V_{acc} the image formation reduces in matrix form to $Y_L = H_L O_L$, where the entries of H_L contain $h_{i,V_{acc}}$ and both Y_L and O_L are vectors whose entries contain respectively the acquired multi-energy BSE images and the deconvolved BSE images.

Equation 2.4 can be solved by deconvolution techniques. In the case of MEDSEM, both H_L and O_L are unknown and the problem is solved by a BSS algorithm. As an illustration of the nontriviality of an ill-posed BSS problem, consider $xy = 1$. Is there a solution that corresponds to the 'true' solution of x and y? The task is now to estimate both H_L and O_L from Y_L subject to a certain noise model to reconstruct the interior of the sample in 3D. This can be achieved by several methods such as independent component analysis[37], sparse principal component analysis[38] and non-negative matrix factorization[39]. The latter has been successfully used by D.A. Fish et al. (1994) for the blind deconvolution of images blurred by a PSF based on the Expectation Maximization Maximum Likelihood (EMML) algorithm[40]. This algorithm was chosen for the deconvolution of the acquired BSE images due to its widespread popularity for solving problems very similar to the image formation in MEDSEM.

2.3 The EMMLTV Algorithm

The EMML algorithm provides an approximate maximum likelihood solution to the BSS problem of the assumed instantaneous mixing image formation in MEDSEM. In the EMML algorithm the data Y_L, which is the number of detected BSEs per pixel per scan time interval per V_{acc}, is modeled as independently distributed random variables subject to Poisson noise[41]. Given this model, the estimators H_L and O_L that best fit Y_L can be derived from statistical principles[41–43].

The EMML algorithm introduces noise on the deconvolved BSE images that gets amplified if the algorithm runs for long iteration times. This can be reduced by implementing the Total Variation (TV) regularization[44, 45]. The TV regularization was introduced by Catté et al. (1992) as a constrained optimization type for denoising images[46]. When incorporated into the EMML algorithm the TV regularization acts as a regularization method on the gradient of the image and removes noise in homogeneous regions while preserving edges. The resulting EMMLTV algorithm solves in an iterative manner the assumed image formation $Y_L = H_L O_L$ for the estimators O_L and H_L from some initialization as given by[43]:

$$
\begin{aligned}
O_L &= O_L. \times H_L^T(Y_L./H_L O_L)./(1 - \lambda TV(O_L)) \\
H_L &= H_L. \times (((Y_L./H_L O_L)^\alpha)O_L^T)^{\omega/\alpha})
\end{aligned}
\tag{2.5}
$$

where point wise multiplication and division denote element wise operations between matrices and vectors, the superscript T denotes the transpose operation, the $TV(O)$ term stands for the calculation of the TV regularization term, λ is the regularization parameter that determines the strength of the regularization, $\omega = 1.9$ is an acceleration exponent to speed up the convergence of the solution[47] and $\alpha = 2$ is a relaxation parameter to improve the stability of the algorithm[48]. An informal derivation of the EMMLTV algorithm is given in Appendix A.

The EMMLTV algorithm achieves the SEM equivalence of optical sectioning methods and enables, under the assumption of the instantaneous mixing model of the image formation, a simple 3D imaging method in the SEM. It does this by simultaneously solves Y_L for both the maximum likelihood estimators O_L and H_L by alternately computing O_L with known H_L and H_L with known O_L until convergence is met. The result is that the acquired multi-energy BSE images are deblurred along the Z-axis. Then, the deconvolved BSE images are the reconstructed depth slices that contain structural information of subsurface layers of the imaged sample, although the reached depth as function of V_{acc} is not yet properly calibrated.

Chapter 3

Methods of MEDSEM

3.1   Sample Set

All samples that are suited for imaging in an ordinary electron microscope can also be imaged with MEDSEM. However, samples that are very thick and that contain features deeply buried under the surface cannot be properly with MEDSEM, since the BSEs cannot access these regions at even the highest V_{acc}. Therefore, a limiting condition is that the samples should not have a structure that varies on large length scales in depth. As a general rule of thumb, samples are restricted by a maximum thickness of around 200 nm, although the actual maximum probing depth also depends on the average density of the material[33–35]. Furthermore, the samples should have some varying structure along the z-direction. Without this the acquired multi-energy BSE images do not contain varying depth information and the deconvolution becomes meaningless. This is also necessary for comparing the deconvolved BSE images with FIBSEM to inspect whether the MEDSEM output agrees with the actual 3D structure of the material and for calibrating the probed depth as function of V_{acc}.

The samples that fulfil the mentioned conditions and that were chosen for this study are Ag@Cu$_2$O core-shell nanowires fabricated in solution as reported by Sciacca et al. (2014)[49] and Au@Cu$_2$O core-shell nanowires fabricated in solution as reported by Kuo et al.[50, 51]. In addition, the synthesis of the Au@Cu$_2$O core-shell nanowires also contains Au sheets as by-products. These are also included in this study in order to try to image particles lying underneath them. After fabrication, the samples are drop-casted on marked Si substrates and imaged in the MEDSEM.

3.2　MEDSEM Workflow

The imaging of nanostructures was performed on a Verios XHR SEM from FEI. For imaging in the BSE mode it contains a Through-the-Lens-Detector (TLD), In-the-Column-Detector (ICD), Mirror-Detector and Concentric-BackScatter Detector (CBSD), which are all indicated in Figure 3.1.
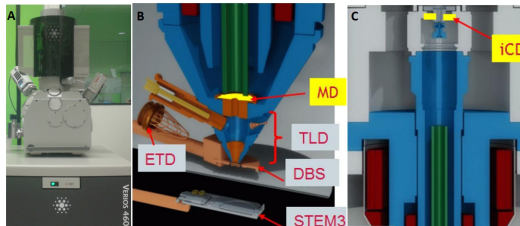

Figure 3.1: *BSE detectors. **A,** Verios XHR SEM. **B,** BSE detectors in the pole piece. The ETD is a secondary electron detector, the STEM3 a transmission electron detector and the DBS stands for the CBSD. **C,** Location of the ICD.*

The workflow of MEDSEM consists out of three steps: acquiring multi-energy BSE images, the deconvolution thereof and the visualization of the deconvolved BSE images. The data acquisition takes place at the most optimal conditions for the electron beam current I_{beam}, pixel dwell time τ_{dwell}, pixel size, V_{acc} range and the number of frame integrations. At these settings the signal-to-noise ratio (SNR) should be sufficiently high while the sample damage is tried to keep minimal. Then, the acquired BSE images are aligned with the FIJI stackreg plugin[52]. The deconvolution is then performed with Matlab by the update rules of equation 2.5. Finally, the deconvolved BSE images are visualized with both MATLAB and FIJI.

The EMMLTV algorithm will be run for a varying number of iterations k and regularization strengths λ for all acquired BSE images to find the optimal deconvolution settings. These are found from the Frobenius norm $||Y_L - H_L O_L||_F$ and the estimated SNR of the deconvolved BSE images at all $[k, \lambda]$ algorithm state points, as shown in Figures 3.2 A and B. The SNR is estimated by applying a 3D-bilateral filter to the deconvolved BSE images[53] and assuming that the filtered deconvolved BSE images, $O_{L,filt}$, are the noiseless signals. Then, the SNR is defined as the ratio between the mean of the filtered signal to the standard deviation of the unfiltered signal:

$$\text{SNR} = \frac{||O_{L,filt}||_F}{||O_{L,filt} - O||_F} \tag{3.1}$$

From a fast convergence of the Frobenius norm, a high SNR and observing the deconvolved depth slices by eye are the optimal deconvolution settings

determined. An example of how several of these act on the deconvolved BSE image of an AgCu$_2$O core-shell nanowire at V_{acc}=16 kV is shown in Figures 3.2 C–F. Figure 3.2 C shows the deconvolved BSE image for k=75 and λ=10^{-3}, the optimal deconvolution settings for this particular sample. Furthermore, Figure 3.2 D shows the result for k=300 and λ=0, which becomes dominated by noise and k is too high. Figure 3.2 E shows how the noise can be significantly reduced by applying the TV regularization for k=300 and λ=10^{-3}. However, Figure 3.2 F shows the result for k=75 and λ=0.1, which is distorted by the strong TV regularization and λ is too high.
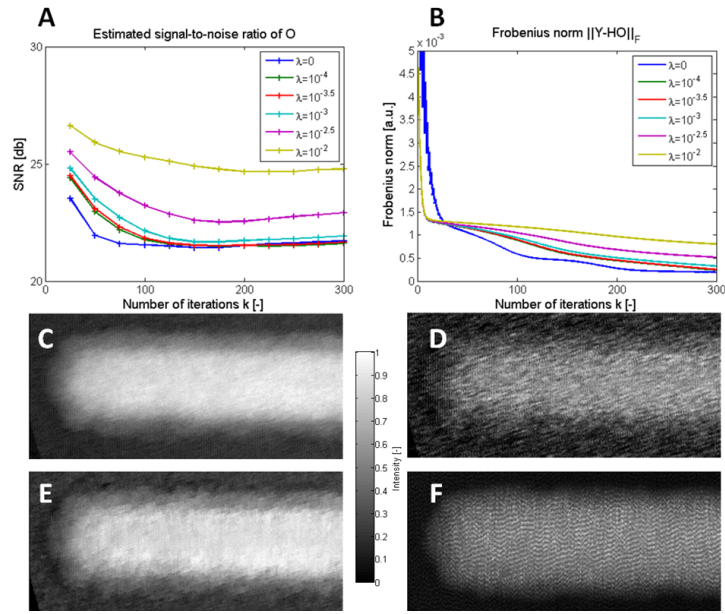
Figure 3.2: *The effects of the deconvolution settings.* ***A,*** *Estimated SNR.* ***B,*** $||Y-HO||_F$. ***C,*** *Deconvolved BSE image for k=75 and λ=10^{-3}.* ***D,*** *Deconvolved BSE image for k=300 and λ=0.* ***E,*** *Deconvolved BSE image for k=300 and λ=10^{-3}.* ***F,*** *Deconvolved BSE image for k=75 and λ=0.1.*

Finally, FIBSEM cross cuts are taken of the samples imaged with MEDSEM. This was done on a Helios NanoLab DualBeam FIB from FEI. By comparing the FIBSEM cross cut with the deconvolved BSE images can the quality of the latter be evaluated, the artifacts introduced by the deconvolution identified and the limits of 3D imaging with MEDSEM determined.

Chapter 4

3D Imaging with MEDSEM

First, a broad overview of imaging Ag@Cu$_2$O core-shell nanowires in 3D with MEDSEM is presented and discussed, together with the main artifacts present in the 3D images and the limited resolving power of MEDSEM. This is followed by presenting and discussing the best MEDSEM results on an Au@Cu$_2$O core-shell nanowire and Au@Cu$_2$O core-shell nanoparticles lying underneath Au sheets. Volume rendered movies of the 3D data of the samples presented in this chapter can be found on `http://www.amolf.nl/to_be_updated`.

4.1   Ag@Cu$_2$O Core-Shell Nanowires
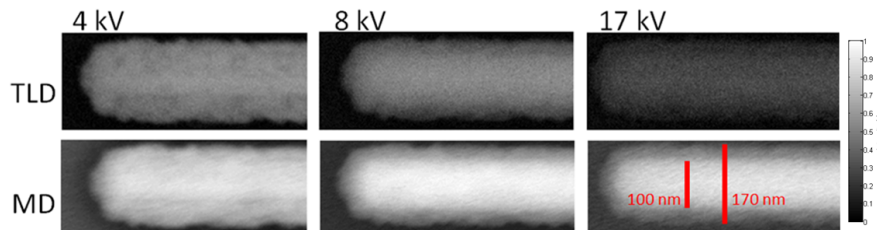
Figure 4.1: *BSE images of an Ag@Cu$_2$O core-shell nanowire. Top row: images obtained with the TLD, bottom row: images obtained with the MD. The columns indicate the applied* V_{acc}*.*

An Ag@Cu$_2$O core-shell nanowire was imaged in the BSE mode for various V_{acc}. The images were obtained at 20 equally spaced V_{acc} in the range V_{acc}=4–23 kV with both the TLD and MD for I_{beam}=0.40 nA, τ_{dwell}=0.60 μs, 8 integrated frames and a pixel size of 1.70×1.70 nm^2. Figure 4.1 shows

both the TLD and MD BSE images at V_{acc}=4, 8 and 17 kV, of which the BSE images at high V_{acc} reveal contrast between two regions. This effect is much stronger for the MD than the TLD.
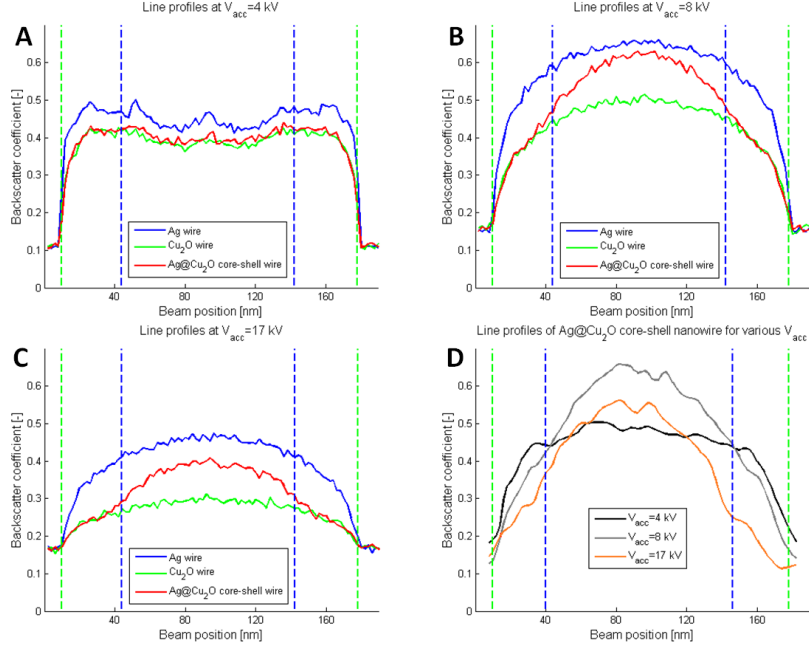
Figure 4.2: *The backscatter coefficient over simulated and real nanowires. The green and blue dashed lines respectively indicate the edge of the shell and core of the simulated Ag@Cu$_2$O core-shell nanowire.* **A,** V_{acc}=4 kV. **B,** V_{acc}=8 kV. **C,** V_{acc}=17 kV. **D,** *Experimental line profiles over an AgCu$_2$O nanowire at various V_{acc}.*

To validate whether this observed contrast is indeed due to the chemical difference between the core and shell of the nanowire, MC calculations of the backscatter coefficient of an Ag nanowire, a Cu$_2$O nanowire and an Ag@Cu$_2$O core-shell nanowire were performed. A total of 100 scan points spaced 2 nm over the nanowire were simulated with 5000 primary beam electrons for each. The MC calculations were then compared with the experimental backscatter coefficient over the long red scale bar in Figure 4.1 and shown in Figure 4.2. At V_{acc}=4 kV, Figure 4.2 A shows that the backscatter coefficient along the whole Ag@Cu$_2$O core-shell nanowire is identical to that of the Cu$_2$O nanowire. The sharp peaks along the nanowires arise from the polyhedral shape of the defined geometry of the nanowires. Increasing V_{acc} to 8 and 17 kV results in an identical backscatter coefficient in the regions between the blue and green dashed lines, the shell region of the Ag@Cu$_@$O core-shell nanowire, for both the Ag@Cu$_2$O and Cu$_2$O nanowires. However,

the core region displays a significantly increased backscatter coefficient, almost reaching that of the Ag nanowire. This steep increase of the backscatter coefficient is also present in the experimental line profiles for V_{acc}= 8 and 17 kV between the blue lines. Given the results of the MC calculations, this indicates that there the composition also contains Ag and that the contrast at high V_{acc} arises from the presence of the Ag core within the nanowire. Therefore, at high V_{acc} the nanowire's depth structure can be probed, since then the BSEs have sufficient energy to penetrate through the shell.

After acquiring multi-energy BSE images the EMMLTV deconvolution algorithm of Equation 2.5 was applied. This was only done for the images obtained with the MD, since the TLD did not provide good elemental contrast. Then, the SNR and $||Y - HO||_F$ were quantified for various regularization strengths λ and iteration lengths k. From the procedure described in Section 3.2 the optimal deconvolution settings were determined to be k=75 and λ=10^{-3}. To visualize the effect of the deconvolution, both the acquired and deconvolved BSE images were stacked on top of each other and cut along either the X or the Y-axis with their gray values inverted and converted to a heat map as shown in Figures 4.3 A–D. A low intensity (black) corresponds to a high backscatter coefficient and all the uncut transparent regions contain the signal from the Si substrate. Furthermore, the XZ and YZ cross cuts of both the acquired and deconvolved BSE images are shown in Figures 4.3 E and F. A FIBSEM cross cut was obtained along the YZ cross cut of Figure 4.3 F and shown in Figure 4.3 G to observe whether the deconvolved BSE images contain depth information that corresponds with the nanowires actual 3D structure. This allowed the determination of the probing depth of the deconvolved BSE images, which is shown in Figure 4.3 H. Then, Figure 4.3 I contains the YZ cross cut of the deconvolved BSE images rescaled along the Z-direction.

The effect of the deconvolution is a sharper separation of the core from the shell. Figures 4.3 A and C show that the acquired BSE images contain a dark region in the middle of the nanowire, corresponding to the Ag core. Figures 4.3 B and D show that this region becomes more well-defined with sharper core-shell interfaces after the deconvolution, indicating more clearly the transition from core to shell within the nanowire's interior. In addition, the deconvolved BSE images show the top part of the Ag core as having a triangular structure. This can also be seen on the acquired BSE images, though there the effect seems to be less clear. Furthermore, both the core and the shell display a slight narrowing on the bottom acquired and deconvolved BSE images. However, both regions do not fully close. Again, this effect is more clear for the deconvolved BSE images. These observed features of the core-shell interface after the deconvolution are also present in the YZ cross

cut in Figure 4.3 F.

The FIBSEM cross cut shows that the deconvolved BSE images contain depth information that qualitatively agrees with the actual 3D structure of the nanowire. Figure 4.3 G shows that the Ag core has a pentagonal structure. This indicates that the deconvolution correctly retrieved the top part of the Ag core's structure. However, the deconvolution could not retrieve the bottom part of the Ag core and the Cu_2O shell. Presumably the largest V_{acc} is too low for the BSEs to fully penetrate through the nanowire and the deconvolved BSE images cannot reconstruct the bottom of the nanowire. Increasing V_{acc} could provide the sufficient energy to image the nanowire's bottom parts in more detail. This puts a limit on the achievable depth information that can be retrieved from a deconvolution of the BSE images.

The determination of the probing depth as function of V_{acc} was done by matching by eye the deconvolved BSE images with the structure of the Ag core on the FIBSEM cross cut. More specifically, the deconvolved BSE image showing the top of the Ag core, the widest part of the Ag core and the last deconvolved BSE image were put on the corresponding depths on the FIBSEM cross cut. Then, the missing voxels were obtained by interpolation from the other deconvolved BSE images. From this, it was found that the deconvolved BSE image at V_{acc}=5 kV, which corresponds to the first signal of the Ag core, lies approximately at a depth of 20 ± 5 nm as measured from the top of the nanowire. Furthermore, the deconvolved BSE image at V_{acc}=12 kV, which corresponds to the widest part of the core, lies at a depth of 60 ± 10 and the final deconvolved BSE image at $_{acc}$=23 kV corresponds to a depth of 110 ± 20. From this analysis, the average obtained resolution in the Z-direction in the Ag core is estimated by dividing the total depth covered by the deconvolved BSE images of the Ag core by their number. This gives an estimated Z-resolution of $\sim 5 \pm 1$ nm and a voxel size of $\sim 1.70 \times 1.70 \times 5 \mathrm{nm}^3$.

Above values are crude estimations and an improved determination of the Z-resolution, together with a larger resolution, could be obtained from acquiring more BSE images at smaller V_{acc} increments in a wider V_{acc} range. This would allow a more precise localization of features in 3D, since smaller transitions will be possible to observe on the acquired, and therefore as well on the deconvolved BSE images. Furthermore, increasing V_{acc} to higher values is necessary to probe deeper into the nanowire for a more complete 3D reconstruction thereof.

Another demonstration of probing the interior of a nanowire from BSE images is presented in Figure 4.4, which shows the MEDSEM results of a thicker Ag@Cu_2O core-shell nanowire with a core diameter of 180 nm and outer diameter of 270 nm was imaged. The unscaled deconvolved BSE images are visualized in Figures 4.4 A–C in the same way as in Figures 4.3 B and
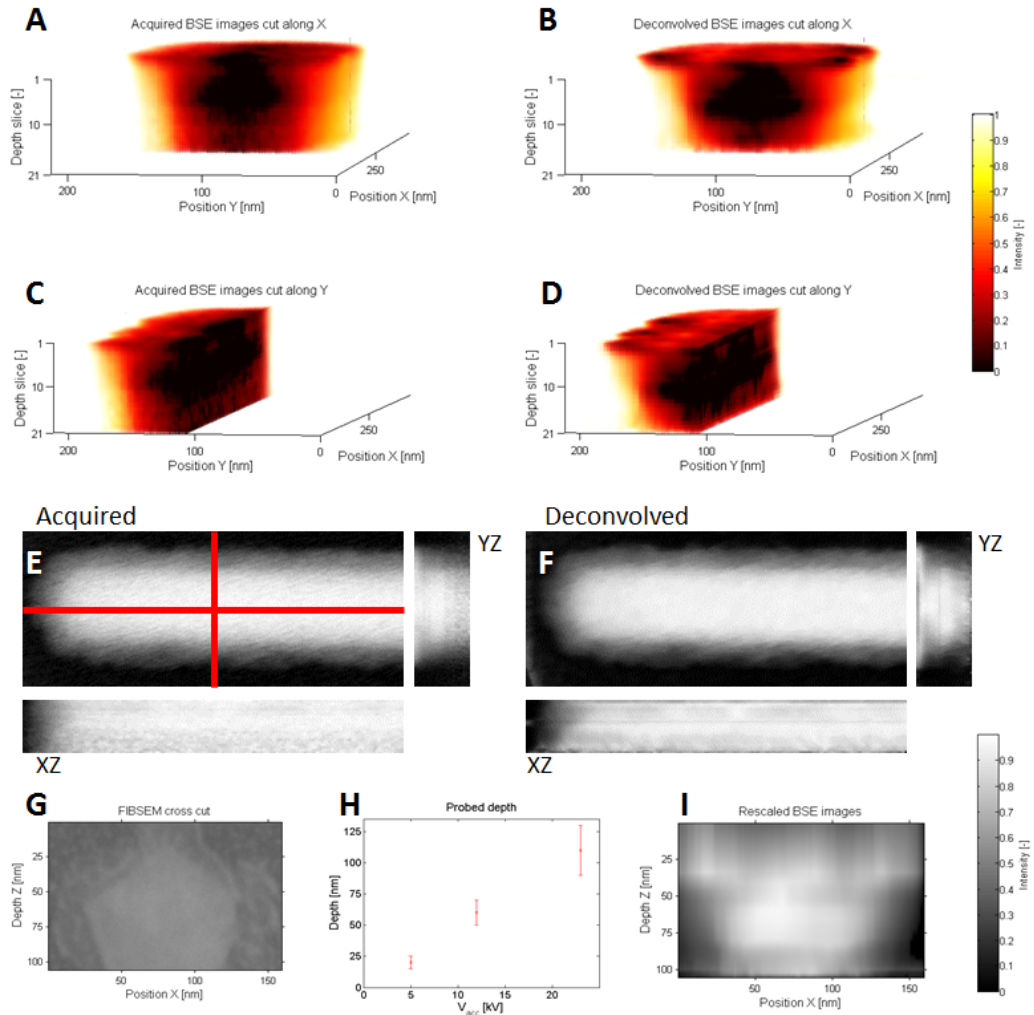
Figure 4.3: *BSE imaging of the 3D structure of an Ag@Cu₂O core-shell nanowire.* **A,** *Acquired BSE images cut along the X-axis.* **B,** *Deconvolved BSE images cut along the X-axis.* **C,** *Acquired BSE images cut along the Y-axis.* **D,** *Deconvolved BSE images cut along the Y-axis.* **E,** *The XZ and YZ cross cuts of the acquired BSE images.* **F,** *The XZ and YZ cross cuts of the deconvolved BSE images.* **G,** *FIBSEM cross cut of the nanowire along the YZ cross cut.* **H,** *Depth probing from the top of the nanowire as function of* V_{acc}. **I,** *The YZ cross cut of the deconvolved BSE images rescaled along the Z-direction according to the probing depth relationship.*

D, but then also cut along the Z-axis. To enhance the visualization of the Ag core, Figure 4.4 D contains isosurfaces that match the intensities of the Cu_2O shell, in green, and the Ag core, in blue. After the deconvolution, the core-shell interface becomes clear in 3D. Furthermore, since this nanowire is thicker than the previous one, depth information can only be obtained of the top part of the nanowire. More importantly, Figures 4.4 B–D show that the Ag core is partially absent in the wire, demonstrating the potential of volumetric chemical characterization of nanostructures from deconvolved BSE images.
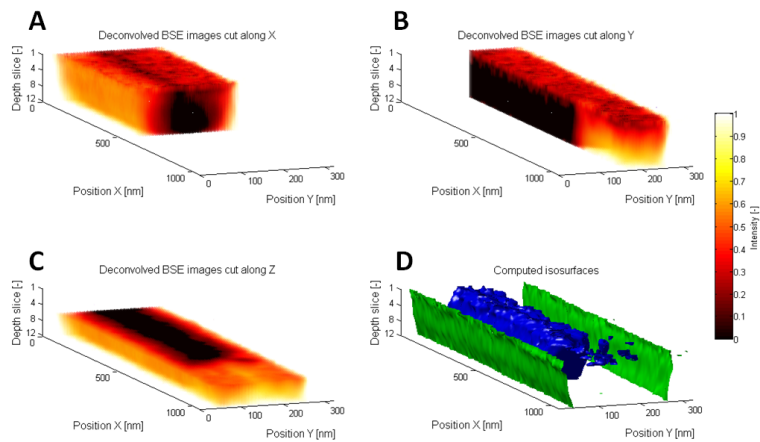
Figure 4.4: *BSE imaging of the 3D structure of a thick $Ag@Cu_2O$ core-shell nanowire.* ***A,*** *Deconvolved BSE images cut along the X-axis.* ***B,*** *Deconvolved BSE images cut along the Y-axis.* ***C,*** *Deconvolved BSE images cut along the Z-axis.* ***D,*** *Computed isosurfaces that match the Ag core and the $Cu_@O$ shell.*

In both presented examples MEDSEM provides qualitative depth information of the top part of the nanowire that does not match its true 3D structure. Figure 4.3 G shows that nanowire's shell also has a pentagonal shape, which could not be retrieved by the deconvolution. There, the top deconvolved BSE images contain strong signals on the edges of the wire where no material should be present. This is a reconstruction artifact that arises from the way in which surface topography is imaged in BSE images.

When the primary beam moves over the sample it cannot discriminate between local height differences thereof. This stems from the good focal depth of a SEM. As a consequence, any height differences in the surface topography are projected on a flat 2D image and essentially lost. This means that at low V_{acc} the acquired BSE images contain a projection of the nanowire's surface over the whole diameter instead of only the top part. The result is that the top deconvolved BSE images contain features at the outer parts of the wire

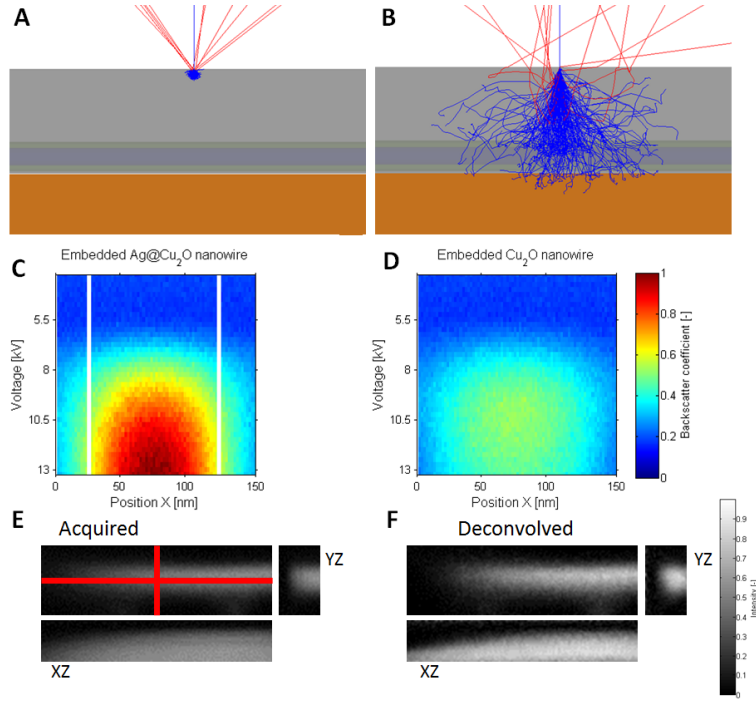Figure 4.5: *Resolving the surface topography artifact. **A,** MC calculation of electron trajectories at $V_{acc}= 3\ kV$. **B,** MC calculation of electron trajectories at $V_{acc}= 6.5\ kV$. **C,** Simulated backscatter coefficient over an embedded $Ag@Cu2_2O$ core-shell nanowire. **D,** Simulated backscatter coefficient over an embedded $Cu2_2O$ nanowire. **E,** The XZ and YZ cross cuts of the acquired BSE images of an $Ag@Cu2_2O$ core-shell nanowire embedded in silica sol-gel. **F,** The XZ and YZ cross cuts of the deconvolved BSE images of that same nanowire.*

where none should be. It is possible to reduce this artifact by embedding the nanowires in a matrix of a different material.

An embedding matrix functions to uniformly slow down the beam at all scan points. Figure 4.5 A and B show MC calculations of electron trajectories (BSEs are red) in a sample containing an $Ag@Cu2_2O$ core-shell nanowire (blue is Ag, green is Cu_2O) on a Si substrate (orange) embedded in a silica sol-gel matrix (gray) at respectively V_{acc}=3 kV and V_{acc}=6.5 kV. In the former the primary beam penetrates only into the top region of the matrix from which the BSEs emerge, whereas in the latter the beam just reaches the top of the nanowire. Then, only the top part of the whole nanowire emits BSEs, whereas all other scan points still produce a background signal of the matrix. By increasing V_{acc} in small steps the imaged part of the nanowire widens, since then BSEs can increasingly penetrate deeper into the matrix and cover more of the nanowire's surface. This is illustrated in Figures 4.5 C

and D, which contain the simulated backscatter coefficient for V_{acc}=3–13 kV at 0.25 kV increments over respectively an Ag@Cu$_2$O core-shell and Cu$_2$O a nanowire. Upon increasing V_{acc} above 6.5 kV, the evolution of the surface topography of the nanowire becomes visible as function of V_{acc}. In addition, the presence of the Ag core in the core-shell nanowire could then still be detected as the increased signal in the core region between the white lines in Figure 4.5 C, which is absent in Figure 4.5 D.

However, experimental attempts at removing the topography artifact were unsuccessful. Three embedding matrices were tried: silica sol-gel, Poly(3,4-ethylenedioxythiophene) Polystyrene sulfonate (PEDOT:PSS) and Poly(methyl methacrylate) (PMMA). Layers with a thickness of 200–600 nm were spin coated on samples containing Ag@Cu$_2$O core-shell nanowires. Figure 4.5 E and F show respectively 22 acquired and deconvolved BSE images at equally spaced V_{acc} in the range V_{acc}= 3–24 kV together with their XZ and YZ cross cuts. The YZ cross cuts provide an improved representation of the nanowire's surface topography, the XZ cross cuts indicate that the left part of the wire is buried more deeply in the matrix. However, the silica sol-gel matrix is non-conductive and most of the electrons remained trapped in the matrix, leading to the build-up of negative charge followed by image distortion effects[54] and even to sample damage. This could not be prevented by acquiring many integrated frames at low I_{beam} and τ_{dwell}. Both the PMMA and PEDOT:PSS matrix, of which the latter is conductive, proved to be unstable under primary beam exposure. This resulted in the matrix being destroyed during the imaging process, thereby inducing nanowire drift and image distortion. Furthermore, embedding the nanowires in any matrix reduces the obtainable resolution, since the electron beam becomes more diffuse prior to reaching the nanowire due to scattering events in the matrix. However, a stable, conducting, light and flat matrix could reduce the surface topography artifact and provide better depth information of a nanowire's 3D structure from BSE images.

In conclusion, qualitative depth information of the Ag core in an Ag@Cu$_2$O core-shell nanowires was obtained from applying a deconvolution to BSE images while assuming an instantaneous mixing image formation model. The deepest probed depth was 110 ± 20 nm at V_{acc}=23 kV, which was limited by the thickness of the wires. The resolution in the Ag core in the Z-direction was estimated at ~ 5 nm. Furthermore, reconstructing the true surface topography of the nanowire was unsuccessful due to the identified topography artifact. Finally, strategies were proposed to improve both the resolution and to resolve the topography artifact.

4.2 Au@Cu$_2$O Core-Shell Nanowire

In addition to the Ag@Cu$_2$O core-shell nanowire, a smaller Au@Cu$_2$O core-shell nanowire was imaged with MEDSEM. In total 35 BSE images were obtained at steps of 0.5 kV in the range V_{acc}= 2–15 and steps of 1 kV in the range V_{acc}=15–23 kV kV with the MD for I_{beam}=0.10 nA, τ_{dwell}=0.90 μs, 8 integrated frames and a pixel size of 0.84×0.84 nm^2. Figures 4.6 A, B and C show respectively the BSE image at V_{acc}=3 kV, which only contains the BSE signal of the Cu$_2$O shell of the nanowire, at V_{acc}=11.5 kV, which shows the Au core, and at V_{acc}=18 kV, which has a lower intensity, indicating that the nanowire starts to become transparent for the primary beam. The optimal deconvolution settings were k= 75 and λ=$10^{-2.5}$. The results are shown in Figures 4.6 D, E, F and G, where the acquired and deconvolved BSE images were stacked on top of each other and cut along the X- and Y-axis with their gray values inverted and converted to a heat map. This is followed by the XZ and YZ cross cuts of the acquired and deconvolved BSE images in Figures 4.6 H and I. Figure 4.6 J shows a FIBSEM cross cut obtained along the YZ cross cut. This was compared with the obtained depth information from the deconvolved BSE images to determine the depth probing thereof, as shown in 4.6 K. Finally, the deconvolved BSE images were rescaled in depth, as shown in Figures 4.6 L.

The deconvolution of the BSE images provides depth information of the nanowire's inner structure. Figures 4.6 A–C demonstrate that the Au core within the nanowire can be observed at high V_{acc}. Figures 4.6 D–G show that the first few acquired and deconvolved BSE images contain only the signal originating from the Cu$_2$O shell. From the BSE images at higher V_{acc}, the deconvolution reconstructs the interior of the nanowire from the blurred combination of the Au core and Cu$_2$O shell along the Z-direction on the acquired BSE images. More specifically, the deconvolution separates the core from the shell in 3D and the core-shell interfaces become well-defined, localized in space and clearly visible. In these graphs, a black and dark red intensity correspond to signal from the Au core. At high V_{acc} the nanowire becomes narrower on the acquired acquired BSE images and the core intensity drops, but does not fully close. On the deconvolved BSE images, the top of the core appears at V_{acc}=5.5 kV and both the bottom of the core and the shell close at respectively V_{acc}=14.5 kV and V_{acc}=19 kV. The final deconvolved BSE images at $V_{acc} \geqslant$ 20 kV only contain a background signal from the substrate and noise. The core-shell interface and the closing of the bottom part of the nanowire can also be observed in the XZ and YZ cross cuts of Figures 4.6 H and I.

The FIBSEM cross cut of Figure 4.6 J shows that the obtained 3D depth
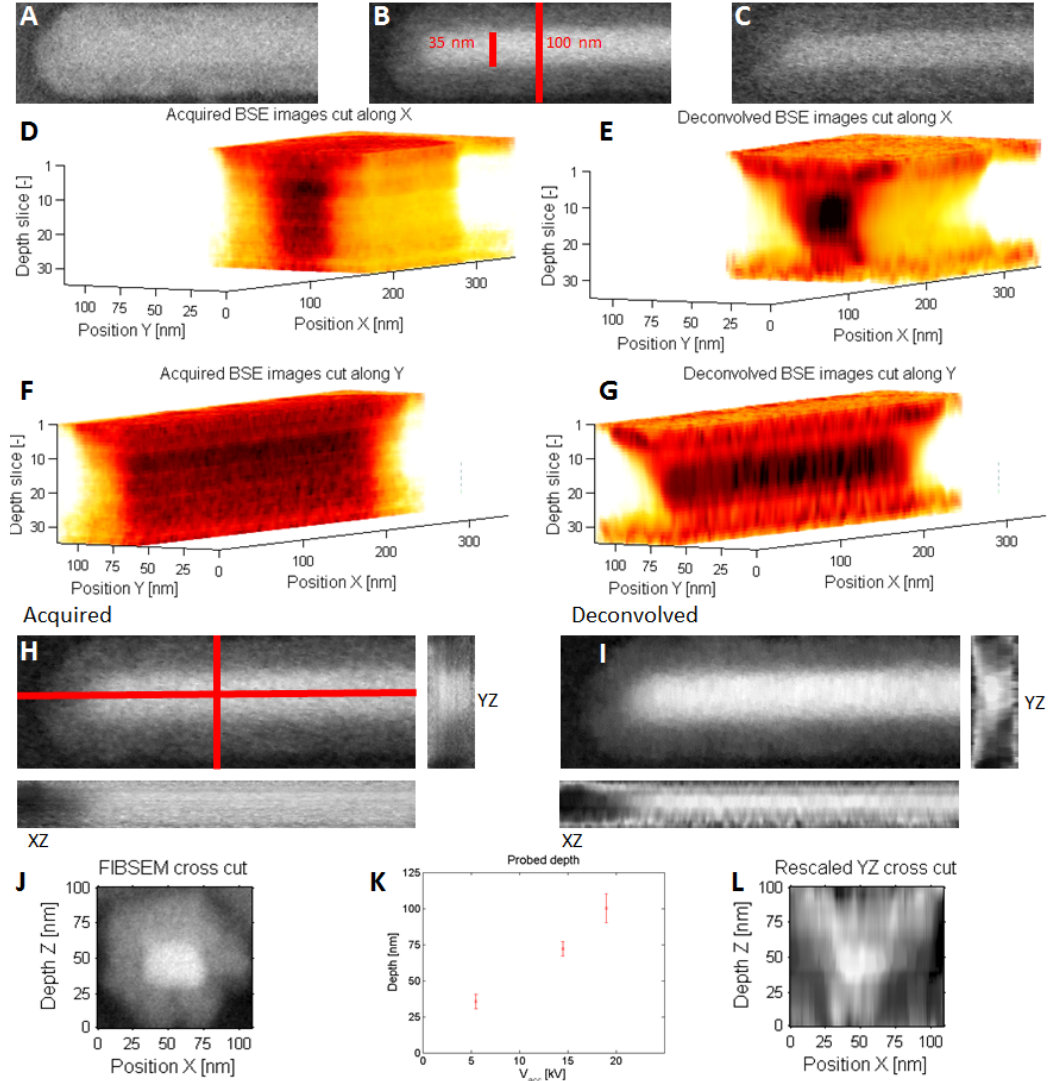
Figure 4.6: *BSE imaging of the 3D structure of an Au@Cu$_2$O core-shell nanowire.* **A,** *Acquired BSE image at V_{acc}=3 kV.* **B,** *Acquired BSE image at V_{acc}=11.5 kV.* **C,** *Acquired BSE image at V_{acc}=18 kV.* **D,** *Acquired BSE images cut along the X-axis.* **E,** *Deconvolved BSE images cut along the X-axis.* **F,** *Acquired BSE images cut along the Y-axis.* **G,** *Deconvolved BSE images cut along the Y-axis.* **H,** *The XZ and YZ cross cuts of the acquired BSE images.* **I,** *The XZ and YZ cross cuts of the deconvolved BSE images.* **J,** *FIBSEM cross cut of the nanowire along the YZ cross cut.* **K,** *Depth probing from top of the nanowire as function of V_{acc}.* **L,** *The YZ cross cut of the deconvolved BSE images rescaled along the Z-direction according to the probing depth relationship.*

22

information of the nanowire from the deconvolved BSE images qualitatively agrees with its actual structure. The core-shell structure and its interface, as retrieved from the deconvolution, is present in the FIBSEM cross cut. However, the topography artifact is present and on the top deconvolved BSE images it appears as if a flat Cu_2O shell spans the whole diameter of the wire, whereas the FIBSEM cross cut indicates a triangular top structure of the shell. Correcting for this topography artifact, as mentioned in section 4.1, could yield a more correct reconstruction of the top structure of the shell to improve the quality of the 3D image from the deconvolution of BSE images.

Both the probing depth of the deconvolved BSE images as function of V_{acc} and estimated depth resolutions were determined from the FIBSEM cross cut. This is done by matching the deconvolved BSE images with the top and bottom of the Au core and with the bottom of the nanowire. A rescaled 3D image is then obtained by interpolating the missing voxels from the deconvolved BSE images. It was found that the deconvolved BSE image at V_{acc}=5.5 kV lies at a depth of 36.0 ± 5.0 nm as measured from the top of the nanowire, the deconvolved BSE image at V_{acc}=14.5 kV lies at a depth of 70 ± 5 nm and the deconvolved BSE image at V_{acc}=19 kV lies at a depth of 98.0 ± 10.0 nm. From these values the resolution in the Z-direction of the deconvolved BSE 3D image was estimated in the regions of top part of the the shell, the core, and the bottom part of the shell in the same manner as in Section 4.1. The top part of the shell has an estimated Z-resolution of $\sim 4.5 \pm 1.0$ nm, the core has an estimated Z-resolution of $\sim 2.0 \pm 0.5$ nm, and bottom part of the shell has an estimated Z-resolution of $\sim 5.6 \pm 1.0$ nm. As was the case with the Ag@Cu_2O core-shell nanowire, the estimated resolutions could be improved by acquiring more BSE imagese at smaller V_{acc} increments over a wider V_{acc} range.

In conclusion, structural information of the interior of an Au@Cu_2O core-shell nanowire was obtained from the deconvolved BSE images. This allowed the reconstruction of both the core-shell interface of the nanowire and the full nanowire in 3D, albeit the top part of the shell is incorrectly reconstructed due to the topography artifact. From a FIBSEM cross cut it was observed that these features agree qualitatively with the actual 3D structure of the nanowire. Furthermore, an estimated depth resolution of ∼2–5 nm was achieved. Finally, the quality and Z-resolution of the 3D image obtained from the deconvolved BSE images could be improved by correcting for the topography artifact and by acquiring BSE images at a better tailored V_{acc} range.

4.3   Imaging through Au Sheets

More complex layered samples were tried to image in 3D with MEDSEM to test its depth probing limits. A first sample is an Au nanowire lying underneath an Au sheet. In total 26 BSE images were obtained at equidistant V_{acc} in the range V_{acc}=2–28 kV with the MD for I_{beam}=0.10 nA, τ_{dwell}=0.90 μs, 8 integrated frames and a pixel size of 2.24×2.24 nm^2. Figures 4.7 A and B show respectively the acquired BSE images at V_{acc}=2 kV and V_{acc}=28 kV, where the latter shows Au particles and an Au nanowire lying underneath the sheets, as well as multiple sheets stacked on top of each other. The optimal deconvolution settings were k=150 and λ=10$^-$3. Due to the difficulty of volume rendering the data because of the sheet on top of the Au sheet samples, 3D images of the deconvolved BSE images were omitted. However, an example of an Au nanowire imaged through an Au sheet was shown in Figure 1.2 F. The XZ and YZ cross cuts of the acquired and deconvolved BSE images are shown in Figures 4.7 C and D. Finally, a FIB cross cut was taken along the YZ crosscut and compared with the YZ cross cut of the deconvolved BSE images in Figure 4.7 E.

The effect of the deconvolution for this sample is to separate the Au sheet from the Au nanowire and the background. Both cross cuts in Figure 4.7 C show that all the acquired BSE images contain a blurred contribution of the signal from the Au sheet. However, the XZ and YZ cross cuts of Figure 4.7 D show that the deconvolved BSE images contain a clear separation between the Au sheet and the substrate underneath it, as indicated by a sharp transition from high (white) to low (black) intensity. On these, the Au sheet is present from the first deconvolved BSE image till the deconvolved BSE image at V_{acc}=9 kV. The deconvolved BSE images for $V_{acc} \geqslant 9$ kV do not contain a contribution of the Au sheet anymore. Furthermore, the deconvolution indicates that the thickness of the Au sheet does not vary significantly along both the XZ and YZ cross cuts, since the intensity transition occurs at the deconvolved BSE image at either V_{acc}=8 kV or V_{acc}=9 kV. Large local variations should be possible to observe by observing the intensity transition on the deconvolved BSE images for different V_{acc}. In addition, the YZ cross cut in Figure 4.7 D shows the separation between the Au sheet and the Au nanowire for V_{acc}=8–9 kV. This V_{acc} at which the separation occurs is the same along the nanowire. Finally, the separation becomes more sharper on the deconvolved YZ cross cut than on the acquired YZ cross cut.

The FIBSEM cross cut in Figure 4.7 E shows that the nanowire indeed lies underneath the Au sheet. Furthermore, the FIBSEM cross cut indicates that the Au sheets has a constant thickness along the cross cut. The probed depth through the Au sheet is 15 ± 2 nm at V_{acc}=9 kV. However, the Au
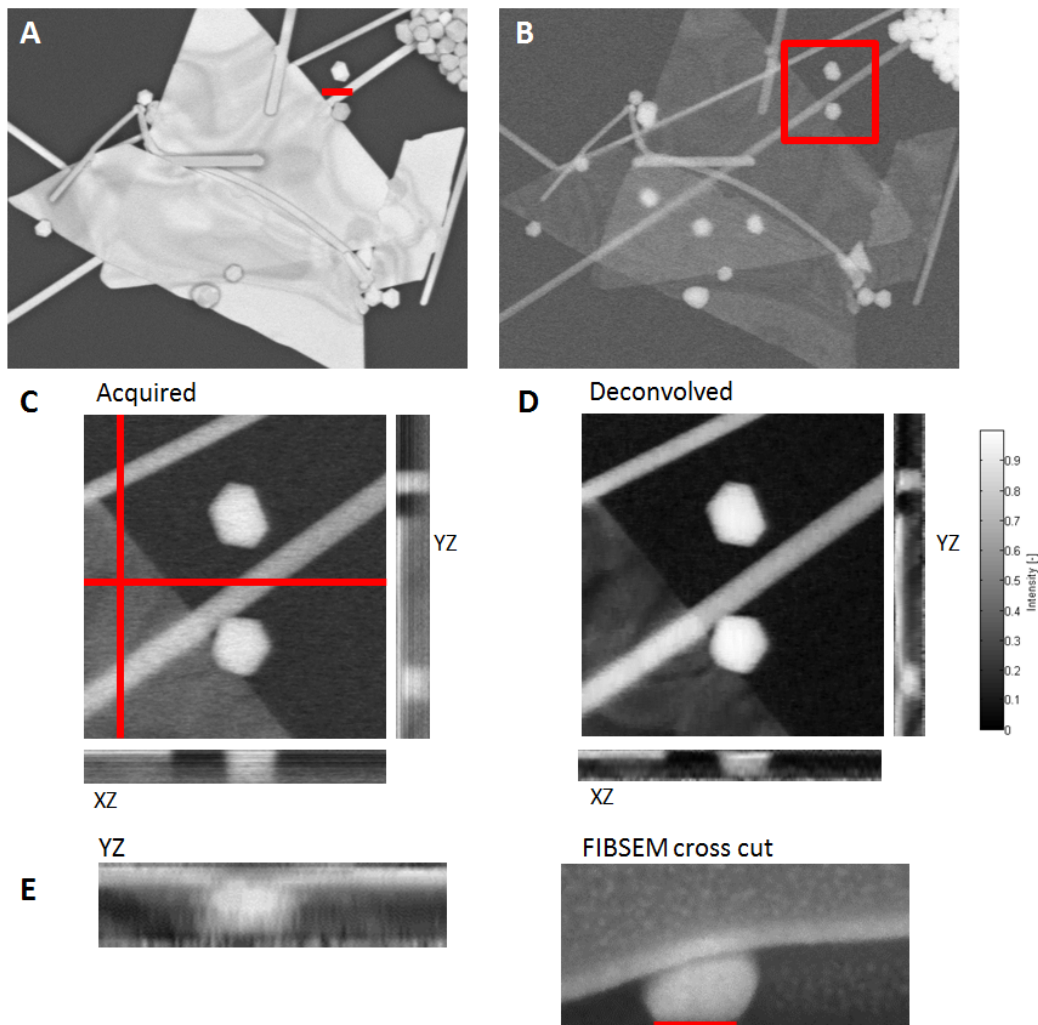
Figure 4.7: *Imaging through an Au sheet.* **A,** *BSE image at V_{acc}=2 kV. The scale bar is 200 nm.* **B,** *BSE image at V_{acc}=28 kV. The red box indicates the region of interest of the next sub-figures.* **C,** *The XZ and YZ cross cuts of the acquired BSE images. The cross cuts are over the red lines.* **D,** *The XZ and YZ cross cuts of the deconvolved BSE images.* **E,** *The YZ cross cut of the deconvolved stack (left) and the FIBSEM cross cut (right). The scale bar is 50 nm.*

sheet is curved and bends down in the left part of the FIBSEM cross cut, which could not be observed from both the acquired and deconvolved BSE images due to the flat projection of the structure on the BSE images.

To test the possibility of obtaining depth information from beneath a thicker Au layer, Au@Cu$_2$O core-shell nanoparticles lying underneath two Au sheets both covered by a Cu$_2$O shell were tried to image with MEDSEM. In
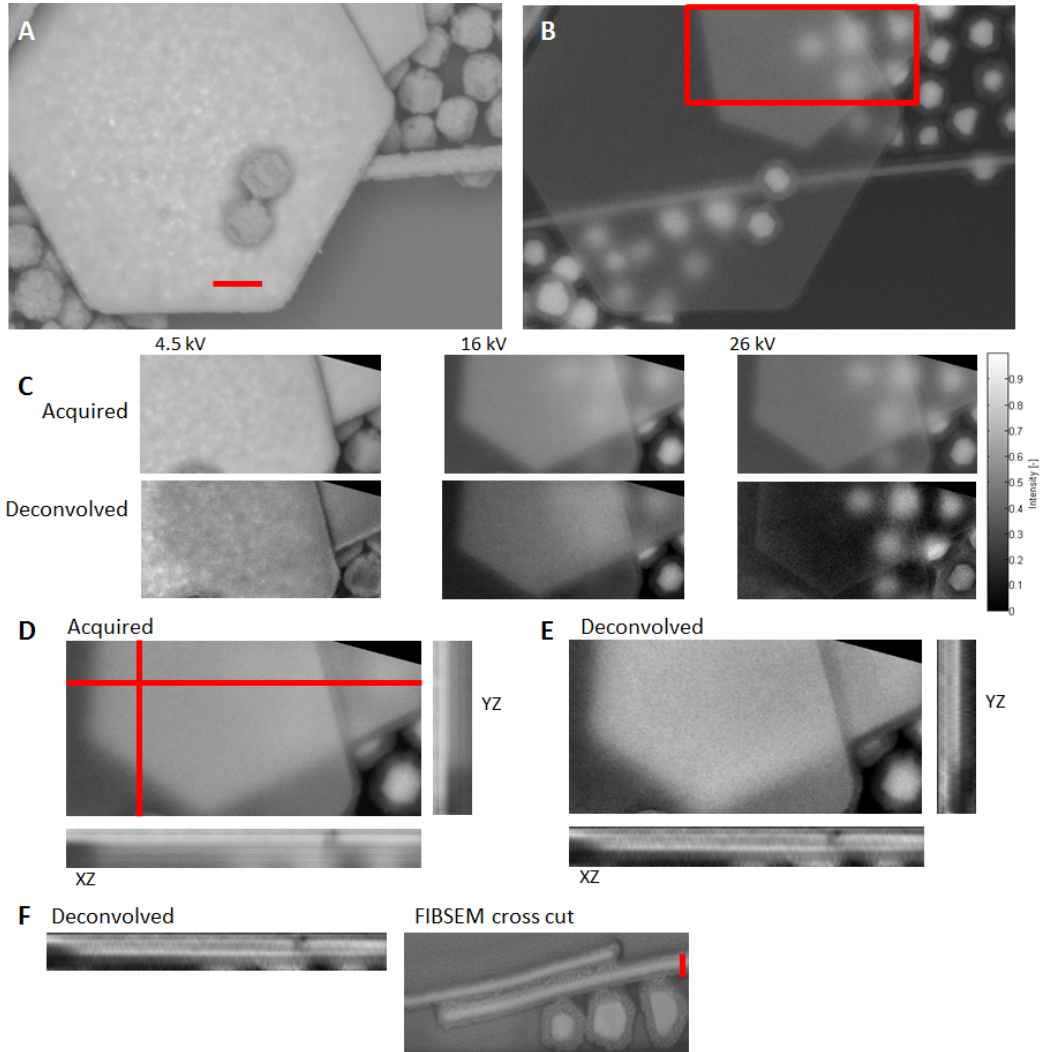
Figure 4.8: *Imaging through two Au sheets. Th scale bar is 200 nm. **A**, BSE image at $V_{acc}=2$ kV. **B**, BSE image at $V_{acc}=29$ kV. The red box indicates the region of interest of the next sub-figures. **C**, Top row, acquired BSE images at $V_{acc}=4.5$, 16 and 26 kV, bottom row, deconvolved BSE images at the same V_{acc}'s. **E**, The XZ and YZ cross cuts of the acquired BSE images. The cross cuts are over the red lines. **F**, The XZ and YZ cross cuts of the deconvolved BSE images. **E**, The YZ cross cut of the deconvolved BSE images (left) and the FIBSEM cross cut (right). The scale bar is 60 nm.*

total of 28 BSE images images were obtained at steps of 0.5 kV in the range $V_{acc}=3$–7 kV, steps of 1 kV in the range $V_{acc}=7$–20 kV and steps of 1.5 kV in the range $V_{acc}=20$–29 kV with the inner ring of the CBSD for $I_{beam}=0.10$ nA, $\tau_{dwell}=0.60$ μs, 8 integrated frames and a pixel size of 0.67×0.67 nm^2. Figures

4.8 A and B show the acquired backscattered electron images at respectively V_{acc}=2 kV and V_{acc}=29 kV. At V_{acc}=2 kV, only the surface topography of the sample is visible, whereas at V_{acc}=29 kV the second Au sheet and Au@Cu$_2$O core-shell nanoparticles and nanowires lying underneath either the first or the second Au sheet can be seen. The optimal deconvolution settings were k=125 and λ=$10^{-2.5}$. A comparison between the acquired and deconvolved BSE images at V_{acc}=4.5, 16 and 26 kV is shown in Figure 4.8 C. The XZ and YZ cross cuts of the acquired and deconvolved BSE images are shown respectively in Figures 4.8 D and E. Finally, a FIB cross cut along the XZ cross cut is compared with the XZ cross cut of the deconvolved BSE images in Figure 4.8.

In this case the deconvolution not only separates the Au sheet from the structures underneath it, but also the two Au sheets from each other. Figure 4.8 C shows that the deconvolved BSE image at V_{acc}=16 kV only contains a contribution of the bottom Au sheet, while the top sheet is still present on the acquired BSE image. Furthermore, the second Au sheet is also removed from the deconvolved BSE image at V_{acc}=26 kV, revealing the particles underneath it, which appear sharper and more localized on the deconvolved BSE image. This is better visualized in Figure 4.8 E, which shows the sharp transition in intensity between the single top sheet and the substrate on the both left part of the XZ cross cut and the bottom part of the YZ cross cut. Furthermore, the regions where both Au sheets lie on top of each other show an intensity drop when the first Au sheet becomes separated from the substrate, followed by a sharp intensity transition from the bottom Au sheet to the substrate at a higher V_{acc}. In contrast, Figure 4.8 D does not show these sharp transitions on both cross cuts and the sheets appear blurred along the Z-direction.

The FIBSEM cross cut in Figure 4.8 F shows that particles indeed lie underneath two Au sheets and that the deconvolved BSE images allow the reconstruction of the stacked structure in 3D. Furthermore, the top Au sheet, which has total thickness of 40±5.0 nm and an Au thickness of 20±2.5 nm, is removed at the deconvolved BSE image at V_{acc}=11 kV and the second Au sheet, which has total thickness of 65±5.0 nm and an Au thickness of 30±2.5 nm, is removed at the deconvolved BSE image at V_{acc}=24.5 kV. Then, at even higher V_{acc}'s the BSEs probe the core-shell particles through an Au and Cu$_2$O mixture with a total thickness of 105±10.0 nm. However, it is then not possible anymore to observe the transition from core to shell of these, presumably because the beam broadening significantly blurs the acquired BSE images and the deconvolution is not capable of retrieving interface features hidden therein. This makes it also impossible to determine how deep the backscattered electrons traveled into these particles.

The 3D reconstruction from the deconvolved BSE images qualitatively agrees with the actual 3D structure, but contains artifacts. Again, the FIB-SEM cross cut shows that the curved geometry of the sheets could not be retrieved by the deconvolution due to the topography artifact. Furthermore, another artifact is visible in the top right part of Figures 4.8 C, D and E, where an area that is only covered by the bottom Au sheet is reconstructed as being very thick after the deconvolution. This part should become transparent between V_{acc}=11 kV and V_{acc}=24.5 kV, since the FIBSEM cross cut shows that it is thicker than the top sheet. The origin of this artifact remains unclear and attempts at removing this have so far been unsuccessful. A possible remedy could be a spatial-dependent PSF, since in the current version of the algorithm the PSF is an average function over the whole sample that dictates the same mixing of deconvolved BSE images at all scan points, whereas it is quite possible that the PSF is different for regions of differing composition and height.

The final, and most complex, sample contains two differently size Au sheets, both covered by a Cu_2O shell, with $Au@Cu_2O$ core-shell particles in between them. In total 34 BSE images were obtained at steps of 0.5 kV in the range V_{acc}=2–10 kV, steps of 1 kV in the range V_{acc}=10–20 kV and steps of 1.5 kV in the range V_{acc}=20–29 kV with the inner ring of the CBSD for I_{beam}=0.40 nA, τ_{dwell}=0.30 μs, 16 integrated frames and a pixel size of 1.1×1.1 nm^2. Figures 4.9 A and B show the acquired BSE images at respectively V_{acc}=2 kV and V_{acc}=23 kV, of which the latter shows the rich variety of nanoparticles, nanowires and sheets hidden underneath the top sheet. The optimal deconvolution settings were k=125 and λ=$10^{-2.5}$ and a comparison between the acquired and deconvolved BSE images at V_{acc}=5.5, 21.5 and 29 kV is shown in Figure 4.9 C. The XZ and YZ cross cuts of both the acquired and deconvolved image stacks are shown respectively in Figures 4.8 D and E. Finally, a FIBSEM cross cut was taken along the horizontal red line of Figure 4.9 D and compared with the XZ cross cut of the deconvolved BSE images.

This sample was too complex for providing correct depth information by MEDSEM. The cross cuts in Figure 4.9 E show a sharp drop in intensity at the deconvolved BSE image at V_{acc}=10 kV, indicating the bottom of the top Au sheet. From the FIBSEM cross cut its total thickness was determined at 15±3 nm with an Au thickness of 8±2nm. The FIBSEM cross cut shows that this sample also has a top sheet with a curved geometry, which could not be reconstructed on the deconvolved BSE images. Furthermore, the XZ cross cut of the deconvolved BSE images for $V_{acc} \geqslant$10 kV does not show a qualitative agreement with the FIBSEM cross cut. Another topography artifact projects the particles as lying at the same depth as the bottom
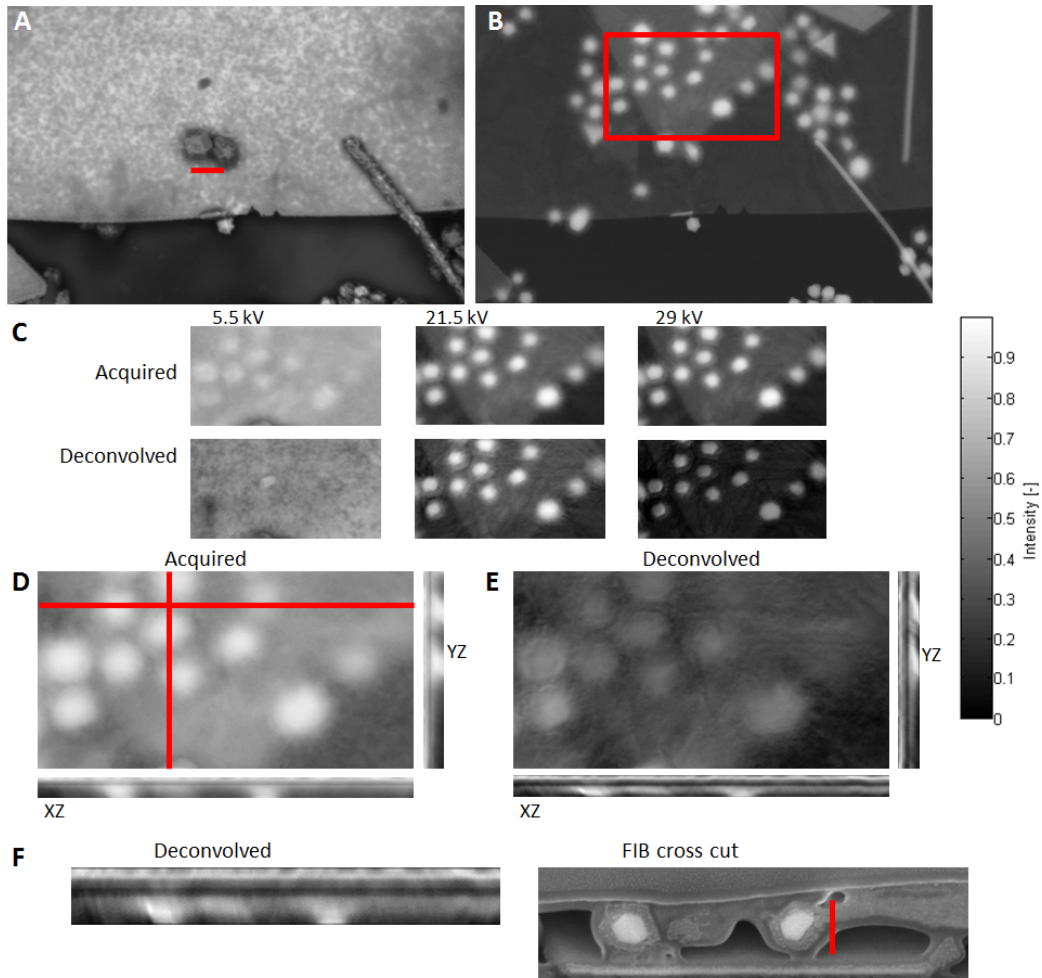
Figure 4.9: *Imaging in between two Au sheets. **A,** BSE image at V_{acc}=2 kV. The scale bar is 200 nm. **B,** BSE image at V_{acc}=23 kV. The red box indicates the region of interest of the next sub-figures. **C,** Top row, acquired BSE images at V_{acc}=5.5, 21.5 and 29 kV, bottom row, deconvolved BSE images at the same V_{acc}'s. **D,** The XZ and YZ cross cuts of the acquired BSE images. The cross cuts are over the red lines. **E,** The XZ and YZ cross cuts of the deconvolved BSE images. **F,** The YZ cross cut of the deconvolved BSE images (left) and the FIBSEM cross cut (right). The scale bar is 200 nm.*

sheet, whereas the FIBSEM cross cut demonstrates otherwise. In this case, whenever the primary beam moves through the top sheet, BSEs emerge from either the bottom sheet or a nanoparticle without discrimination between which object lies higher than the other. However, upon increasing V_{acc} beyond 26 kV the primary beam penetrates through the bottom sheet, which has total thickness of 50±5 nm and an Au thickness of 20±3 nm, at locations

where no particles are present. The result is that the 3D reconstruction locally shows the correct separation of both sheets whenever particles between them are absent, whereas at locations containing a particle the deconvolved BSE images contain a distorted 3D structure. As a result, only qualitatively correct information of the top sheet was obtained and the geometry of the structures lying beneath the top sheet were too complicated for being correctly reconstructed by MEDSEM.

In conclusion, structures lying underneath Au sheets can be imaged with MEDSEM. Furthermore, the deconvolution of multi-energy BSE images can provide insight in the stacked order of sheet-particle and sheet-sheet-particle geometries. In these systems, the deconvolution of multi-energy BSE images can separate the sheets from each other and from the particles. This allowed the visualization of particles lying underneath up to $\sim$100 nm of material for $V_{acc} \geqslant$26 kV.

Chapter 5

Conclusions and Outlook

5.1 Conclusions

The work presented in this thesis demonstrates that non-destructive structural characterization and the retrieval of depth information of nanostructures becomes possible by applying MEDSEM, a simple SEM method that only requires imaging in the BSE mode at different primary beam energies. This can be realized by assuming an instantaneous mixing model for BSE image formation and by accordingly applying a deconvolution to the acquired multi-energy BSE images. While doing so, features that appear blurred along the depth on the multi-energy BSE image stack can be resolved more in clearly in a 3D reconstruction of the nanostructure. This is achieved for several nanostructures.

First, the Ag core of an Ag@Cu$_2$O core-shell nanowire can be visualized with MEDSEM. It is possible to reveal the pentagonal structure of the top of the core in 3D and to probe the nanowire's interior down to a depth of 110 ± 20 nm by applying acceleration voltage's V_{acc} in the range 4–23 kV. Second, the core-shell interface of an Au@Cu$_2$O core-shell nanowire together with its full 3D structure, which has a height of 98 ± 10 nm, can be reconstructed by MEDSEM at nanometer length scales by applying V_{acc}'s in the range 2–24 kV. Finally, particles lying beneath either one or two sheets with total thicknesses in the range 15–100 nm can be imaged with MEDSEM.

The results obtained with MEDSEM provide depth information that qualitatively agrees with the actual structure obtained with FIBSEM cross cuts. However, the topography of the nanostructures can not be correctly reconstructed from the BSE images. A method to correct for this is to embed the nanostructures in a matrix, such that local height variations of the topography become visible on multi-energy BSE images.

5.2 Outlook

This study presented the first steps towards the realization of non-destructive 3D imaging of nanostructures by MEDSEM. More importantly, possible future improvements of the quality of MEDSEM were foreseen.

First, one could attempt to understand in more detail the fundamentals of the image formation. For example, under what conditions does the linearized image formation model hold and can the point-spread-function of a system be determined a priori? Extensive MC calculations of BSE trajectories in a variety of systems of varying compositions and geometries at varying V_{acc} could provide more insight thereof. Furthermore, this could offer a better justification for the usage of the EMMLTV algorithm or suggest even more suited deconvolution techniques. Finally, obtaining a system's PSF from MC calculations will significantly reduce the complexity of the deconvolution problem and could lead to the better retrieval of the 3D structure.

Furthermore, some next experimental steps should be carried out. A first aim could be to try imaging a larger variety of nanostructures and compositions to determine to what extend depth information can be obtained thereof. A second aim is to improve the depth resolution by acquiring more BSE images at smaller increments over a wide V_{acc} range. In addition to this, reaching V_{acc}'s up to 60 kV would fit in well with this approach and reaching deeper probing depths could be a significant extension of MEDSEM. Finally, more effort is required to resolve the topography artifact. This requires embedding the nanostructures in a flat, light, conductive matrix that can slow down the primary beam prior to landing on the sample. A combination of the latter two could significantly improve the 3D imaging capabilities of MEDSEM.

Finally, the deconvolution could be improved in multiple ways. For instance, the EMMLTV algorithm estimates an average PSF over the whole sample that dictates the same mixing at all voxels, whereas regions of different composition and height might have a different PSF. This could be resolved by applying a position-dependent deconvolution that can decouple the mixing process in various regions. However, this significantly increases the computational cost, since then the deconvolution involves the fitting of the 4-dimensional kernel. Another related improvement could be the introduction of a spatially varying λ proposed by L. Yan et al. (2012)[55]. This approach has the benefit that regions that need more TV regularization, such as areas containing a lot of noise, get enough smoothing, whereas other regions that do not require this will be less distorted.

However, the largest shortcoming of MEDSEM is the usage of a blind deconvolution. This cannot guarantee that the obtained solution matches

the true 3D structure of the sample. The simplest method of improving the deconvolution is by reducing the 'blindness' of the problem by introducing new information. This could be in the form of supplying the algorithm with constraints on the geometry of the reconstruction from observed features of the sample during the acquisition stage. For example, the sample could be imaged under various tilting angles and the obtained 3D information of the sample's topography and surface structure could restrict possible outcomes of the deconvolved BSE images. Furthermore, incorporation of the results of MC calculations in the algorithm could serve the same goal, where MC calculations of BSE trajectories performed on the deconvolved BSE images could indicate whether the output is in agreement with the acquired BSE images.

These discussed improvements could be combined in an ideal future MEDSEM platform. Such a platform would provide the user with choice on the deconvolution algorithm, or even an comparison between results of various algorithms. Furthermore, the algorithm should contain self-learning features that in a iterative manner compare deconvolution results with MC simulations and vice versa, while allowing the user to either guess or define geometries or chemical compositions of certain regions. Implementing these could significantly enhance the quality of 3D imaging with MEDSEM.

Bibliography

[1] M. B. Ahrens, M. B. Orger, D. N. Robson, J. M. Li, and P. J. Keller. Whole-brain functional imaging at cellular resolution using light-sheet microscopy. *Nat Meth*, 10(5):413–420, 2013.

[2] R. Erni, M. D. Rossell, C. Kisielowski, and U. Dahmen. Atomic-Resolution Imaging with a Sub-50-pm Electron Probe. *Phys. Rev. Lett.*, 102:096101–096101.

[3] W. Denk and H. Horstmann. Serial Block-Face Scanning Electron Microscopy to Reconstruct Three-Dimensional Tissue Nanostructure. *PLoS Biol*, 2(11):e329, 10 2004.

[4] G. E. Thompson, T. Hashimoto, X. L. Zhong, M. Curioni, X. Zhou, P. Skeldon, P. J. Withers, J. A. Carr, and A. G. Monteith. Revealing the three dimensional internal structure of aluminium alloys. *Surf. Interface Anal.*, 45(5):1535–1542, 2013.

[5] D. Wei, S. Jacobs, S. Modla, S. Zhang, C. L. Young, R. Cirino, J. Caplan, and K. Czymmek. High-resolution three-dimensional reconstruction of a whole yeast cell using focused-ion beam scanning electron microscopy. *Biotechniques*, 53(1):41–48, 2012.

[6] A. Zankel, J. Wagner, and P. Poelt. Serial sectioning methods for 3D investigations in materials science. *Micron*, 62:66–78, 2014.

[7] J. Schweitzer. Scanning Electron Microscopy. `http://www.purdue.edu/ehps/rem/rs/sem.htm`.

[8] S. Van Aert, K. J. Batenburg, M. D. Rossell, R. Erni, and G. Van Tendeloo. Three-dimensional atomic imaging of crystalline nanoparticles. *Nature*, 470:374–377, 2011.

[9] G. Haberfehlner, R. Serra, D. Cooper, S. Barraud, and P. Bleuet. 3D spatial resolution improvement by dual-axis electron tomography: Application to tri-gate transistors. *Ultramicroscopy*, 136:144 – 153, 2014.

[10] P.A. Midgley and M. Weyland. 3D electron microscopy in the physical sciences: the development of Z-contrast and EFTEM tomography. *Ultramicroscopy*, 96(3-4):413–431, 2003. Proceedings of the International Workshop on Strategies and Advances in Atomic Level Spectroscopy and Analysis.

[11] FEI Announces TENEO VS for 3D Volume Imaging of Cells and Tissues. `http://investor.fei.com/releasedetail.cfm?ReleaseID=868814`, 2014.

[12] F. Boughorbel, C. S. Kooijman, B. H. Lich, and E. G. T. Bosch. SEM imaging method. US 8232523B2, 2012.

[13] F. Boughorbel, E. G. T. Bosch, C. S. Kooijman, B. H. Lich, and A. F. de Jong. Charged particle microscopy imaging method. US 8581189B2, 2013.

[14] F. Boughorbel, P. Potocek, C. S. Kooijman, and B. H. Lich. Charge-particle microscope providing depth-resolved imagery. US 8586921B22, 2013.

[15] N. Murata, S. Ikeda, and A. Ziehe. An approach to blind source separation based on temporal structure of speech signals. *Neurocomputing*, 41(1-4):1–24, 2001.

[16] V. D. Calhoun, T. Adali, G. D. Pearlson, and J. J. Pekar. A method for making group inferences from functional MRI data using independent component analysis. *Hum. Brain Mapp.*, 14(3):140–151, 2001.

[17] D. Nuzillard and A. Bijaoui. Blind source separation and analysis of multispectral astronomical images. *Astron. Astrophys. Suppl. Ser.*, 147(1):129–138, 2000.

[18] R. A. Neher, M. Mitkovski, F. Kirchhoff, E.Neher, F. J. Theis, and A. Zeug. Blind Source Separation Techniques for the Decomposition of Multiply Labeled Fluorescence Images. *Bipphysical Journal*, 96(9):3791–3800, 2009.

[19] A. K. Takahata, E. Z. Nadalin, L. T. Duarte, R. Suyama, R. R. Lopes, J. M. T. Romano, and M. Tygel. Unsupervised Processing of Geophysical Signals: A Review of Some Key Aspects of Blind Deconvolution and Blind Source Separation. *Signal Processing Magazine*, 29(4):27–35, 2012.

[20] E. Rutherford. The Scattering of alpha and beta rays by Matter and the Structure of the Atom. *Philos. Mag.*, 6, 1911.

[21] R. Hofstadter, H. R. Fechter, and J. A. McIntyre. High-Energy Electron Scattering and Nuclear Structure Determinations. *Phys. Rev.*, 92:978–987, Nov 1953.

[22] D. Drouin, P. Hovington, and R. Gauvin. CASINO: A new Monte Carlo code in C language for electron beam interactions–part II: Tabulated values of the Mott cross section. *Scanning*, 19(1):20–28, 1997.

[23] N. F. Mott. The Scattering of Fast Electrons by Atomic Nuclei. *Proceedings of the Royal Society of London. Series A*, 124(794):425–442, 1929.

[24] N. F. Mott. The polarisation of electrons by double scattering. *Proceedings of the Royal Society of London. Series A*, 135(827):429–458, 1932.

[25] M. J. Boschini, C. Consolandi, M. Gervasi, S. Giani, D. Grandi, V. Ivanchenko, P. Nieminem, S. Pensotti, P. G. Rancoita, and M. Tacconi. An expression for the Mott cross section of electrons and positrons on nuclei with Z up to 118 ", journal = "Radiation Physics and Chemistry. 90:39–66, 2013.

[26] H. Bethe. Zur theorie des durchgangs schneller korpuskularstrahlen durch materie. *Annalen der Physik*, 397(3):325–400, 1930.

[27] S. Luo, X. Zhang, and D. C. Joy. Experimental determinations of electron stopping power at low energies. *Radiation Effects and Defects in Solids*, 117(1-3):235–242, 1991.

[28] M. Berger and S. Seltzer. Tables of energy-losses and ranges of electrons and positrons. *Studies in penetration of charged particles in matter*, (39):205, 1964.

[29] P. Hovington, D. Drouin, and R. Gauvin. CASINO: A new Monte Carlo code in C language for electron beam interaction–Part I: Description of the program. *Scanning*, 19(1):1–14, 1997.

[30] P. Hovington, D. Drouin, R. Gauvin, D. C. Joy, and N. Evans. CASINO: A new Monte Carlo code in C language for electron beam interactions–Part III: Stopping power at low energies. *Scanning*, 19(1):29–35, 1997.

[31] D. Drouin, A. R. Couture, D. Joly, X. Tastet, V. Aimez, and R. Gauvin. CASINO V2. 42–A Fast and Easy-to-use Modeling Tool for Scanning Electron Microscopy and Microanalysis Users. *Scanning*, 29(3):92–101, 2007.

[32] H. Demers, N. Poirier-Demers, A. R. Couture, D. Joly, M. Guilmain, N. de Jonge, and D. Drouin. Three-dimensional electron microscopy simulation with the CASINO Monte Carlo software. *Scanning*, 33(3):135–146, 2011.

[33] E. H. Darlington. Backscattering of 10-100 kev electrons from thick targets. *Journal of Physics D: Applied Physics*, 8(1):85, 1975.

[34] K. Murata. Spatial distribution of backscattered electrons in the scanning electron microscope and electron microprobe. *Journal of Applied Physics*, 45(9):4110–4117, 1974.

[35] K. Kanaya and S. Okayama. Penetration and energy-loss theory of electrons in solid targets. *Journal of Physics D: Applied Physics*, 5(1):43, 1972.

[36] H. Niedrig and E. I. Rau. Information depth and spatial resolution in {BSE} microtomography in {SEM}. *Nuclear Instruments and Methods in Physics Research Section B: Beam Interactions with Materials and Atoms*, 142(4):523 – 534, 1998.

[37] A. Hyvärinen and E. Oja. Independent component analysis: algorithms and applications. *Neural networks*, 13(4):411–430, 2000.

[38] H. Zou, T. Hastie, and R. Tibshirani. Sparse principal component analysis. *Journal of Computational and Graphical Statistics*, 15(2):265–286, 2006.

[39] D. D. Lee and H. S. Seung. Algorithms for non-negative matrix factorization. In *Advances in neural information processing systems*, pages 556–562, 2001.

[40] D. A. Fish, A. M. Brinicombe, E. R. Pike, and J. G. Walker. Blind deconvolution by means of the richardson–lucy algorithm. *JOSA A*, 12(1):58–65, 1995.

[41] N. Dey, L. Blanc-Feraud, C. Zimmer, P. Roux, Z. Kam, J. Olivo-Marin, and J. Zerubia. Richardson–Lucy algorithm with total variation regularization for 3D confocal microscope deconvolution. *Microscopy research and technique*, 69(4):260–266, 2006.

[42] W. H. Richardson. Bayesian-based iterative method of image restoration. *JOSA*, 62(1):55–59, 1972.

[43] N. Dey, L. Blanc-Féraud, C. Zimmer, P. Roux, Z. Kam, J. Olivo-Marin, and J. Zerubia. 3D microscopy deconvolution using Richardson-Lucy algorithm with total variation regularization. 2004.

[44] T. F. Chan and C. Wong. Total variation blind deconvolution. *Image Processing, IEEE Transactions on*, 7(3):370–375, 1998.

[45] S. Osher, M. Burger, D. Goldfarb, J. Xu, and W. Yin. An iterative regularization method for total variation-based image restoration. *Multiscale Modeling & Simulation*, 4(2):460–489, 2005.

[46] F. Catté, P. Lions, J. Morel, and T. Coll. Image selective smoothing and edge detection by nonlinear diffusion. *SIAM Journal on Numerical analysis*, 29(1):182–193, 1992.

[47] H. Lantéri, M. Roche, O. Cuevas, and C. Aime. A general method to devise maximum-likelihood signal restoration multiplicative algorithms with non-negativity constraints. *Signal Processing*, 81(5):945–974, 2001.

[48] A. Cichocki, S. Cruces, and S. Amari. Generalized alpha-beta divergences and their application to robust nonnegative matrix factorization. *Entropy*, 13(1):134–170, 2011.

[49] B. Sciacca, S. A. Mann, F. D. Tichelaar, H. W. Zandbergen, M. A. van Huis, and E. C. Garnett. Solution-phase epitaxial growth of quasi-monocrystalline cuprous oxide on metal nanowires. *Nano letters*, 2014.

[50] D. Seo, J. H. Park, J. Jung, S. M. Park, S. Ryu, J. Kwak, and H. Song. One-dimensional gold nanostructures through directed anisotropic overgrowth from gold decahedrons. *The Journal of Physical Chemistry C*, 113(9):3449–3454, 2009.

[51] C. Kuo, T. Hua, and M. H. Huang. Au Nanocrystal-Directed Growth of Au- Cu2O Core- Shell Heterostructures with Precise Morphological Control. *Journal of the American Chemical Society*, 131(49):17871–17878, 2009.

[52] P. Thevenaz, U. E. Ruttimann, and M. Unser. A pyramid approach to subpixel registration based on intensity. *IEEE Transactions on Image Processing*, 7(1):27–41, 1998.

[53] Sylvain Paris and Frédo Durand. A fast approximation of the bilateral filter using a signal processing approach. In *Computer Vision–ECCV 2006*, pages 568–580. Springer, 2006.

[54] T. J. Shaffner and R. D. Van Veld. Charging effects in the scanning electron microscope. *Journal of Physics E: Scientific Instruments*, 4(9):633, 1971.

[55] L. Yan, H. Fang, and S. Zhong. Blind image deconvolution with spatially adaptive total variation regularization. *Optics letters*, 37(14):2778–2780, 2012.

Appendix

Derivation of the EMMLTV Algorithm

This appendix contains a brief informal derivation of the EMMLTV algorithm that is applied in MEDSEM to deblur the acquired BSE images along Z-direction to estimate the interior of the imaged sample. This derivation is by no means complete and only serves as an example of how, from statistical principles, Equation 2.5 can be obtained. A complete and formal derivation can be found in [43].

As discussed in Section 2.2, the formation of a BSE image is given by the convolution:

$$Y_{V_{acc}}(x, y) = H_{V_{acc}}(x, y, z) * O(x, y, z) \tag{1}$$

where the data Y is modelled as independently distributed Poisson variables $\text{Pois}\{H_{V_{acc}}(x, y, z) * O(x, y, z)\}$[41]. From now on the PSF will be abbreviated as H, which refers to the beam broadening in 3D as function of location in the sample and V_{acc}. Then, the maximum likelihood of observing Y conditioned on $H * O$ is given by:

$$P(Y|H * O) = \prod_{\mathbf{r}} \frac{[(H * O)(\mathbf{r})]^{Y(\mathbf{r})} e^{-(H*O)(\mathbf{r})}}{Y(\mathbf{r})!} \tag{2}$$

where the product extends over all the spatial indices $\mathbf{r}$ of the matrices Y, H and O.

Minimizing the negative logarithm of Equation 2 with respect to $H * O$ corresponds to finding the most likely $H * O$ that could have generated the observed data Y. The function to minimize then becomes:

$$-\log P(Y|H * O) = \sum_{\mathbf{r}} [(H * O)(\mathbf{r}) - Y(\mathbf{r}) \log((H * O)(\mathbf{r})) + \log(Y(\mathbf{r})!)] \tag{3}$$

The last term of Equation 3 drops out since it is constant with respect

to $H * O$. Combining this with approximating the summation by an integral over $\mathbf{r}$ gives, up to a multiplicative factor, the following cost function:

$$J = \int_{\mathbf{r}} [(H * O)(\mathbf{r}) - Y(\mathbf{r}) \log(H * O)(\mathbf{r})] \mathrm{d}\mathbf{r} \quad (4)$$

Equation 4 needs to be minimized with respect to both H and O. As an example of this procedure, consider a small matrix perturbation $\rho O'$ in O. The new cost function becomes:

$$
\begin{aligned}
J(O + \rho O') &= \int_{\mathbf{r}} [(H * (O + \rho O'))(\mathbf{r}) - Y(\mathbf{r}) \log(H * (O + \rho O')(\mathbf{r}))] \mathrm{d}\mathbf{r} \\
&\cong J(O) + \rho \int_{\mathbf{r}} \left[(H * O')(\mathbf{r}) - Y(\mathbf{r}) \frac{(H * O')(\mathbf{r})}{(H * O)(\mathbf{r})} \right] \mathrm{d}\mathbf{r} \quad (5)
\end{aligned}
$$

The derivative of J with respect to O, $\nabla_O J$, is then, up to some numerical factor, the difference between Equation 5 and Equation 4 for $\lim_{O' \to 0}$. Algebraic manipulation then gives for $\nabla_O J$:

$$\nabla_O J = \int_{\mathbf{r}} H(-\mathbf{r}) \mathrm{d}\mathbf{r} - H(-\mathbf{r}) * \frac{Y(\mathbf{r})}{(H * O)(\mathbf{r})} \quad (6)$$

Taking the value of the integral equal to 1 and solving for 0 yields:

$$H(-\mathbf{r}) * \frac{Y(\mathbf{r})}{(H * O)(\mathbf{r})} = 1 \quad (7)$$

Equation 7 can be solved in an iterative multiplicative manner by assuming that convergence occurs at $\frac{O_{k+1}}{O_k} = 1$ for $\lim_{k \to \infty}$ by:

$$O_{k+1} = O_k \left[H(-\mathbf{r}) * \frac{Y(\mathbf{r})}{(H * O)(\mathbf{r})} \right] \quad (8)$$

Equation 8 gives an iterative update rule of O that maximizes the maximum likelihood function as defined in Equation 2. By applying a matrix perturbation to H in Equation 5 and repeating a similar minimization of J with respect to H, the following iterative update rule of H can be found:

$$H_{k+1} = H_k \left[\frac{Y(\mathbf{r})}{(H * O)(\mathbf{r})} * O(-\mathbf{r}) \right] \quad (9)$$

Finally, Equations 8 and 9 can be rewritten in a matrix formalism corresponding to the linearized form of the BSS problem of image formation in the MEDSEM:

$$O_L = O_L. \times H_L^T(Y_L./H_LO_L)$$
$$H_L = H_L. \times (Y_L./H_LO_L)O_L^T \tag{10}$$

where point wise multiplication and division denote element wise operations between matrices[48]. The EMML algorithm solves Y_L for both O_L and H_L by alternately computing O_L with known H_L and H_L with known O_L from some initialization until convergence is met.

Equation 10 is the unregularized EMML algorithm. The inclusion of the TV regularization is achieved by adding a new term J_{TV} to Equation 4:

$$\begin{aligned} J &= \int_{\mathbf{r}}[(H * O)(\mathbf{r}) - Y(\mathbf{r})\log(H * O)(\mathbf{r})]\mathrm{d}\mathbf{r} + \lambda \int_{\mathbf{r}}|\nabla O(\mathbf{r})|\,\mathrm{d}\mathbf{r} \\ &= J_0 + J_{TV} \end{aligned} \tag{11}$$

where λ is the regularization strength.

Since J_{TV} is independent of H, it is only necessary to find a new update rule for O by minimizing Equation 11 with respect to O. This is achieved by applying a perturbation $\rho O'$ to O in the J_{TV} term of Equation 11 :

$$J_{TV}(O + \rho X') \cong J_{TV}(O) - \rho\lambda \int_{\mathbf{r}} \mathrm{div}\left(\frac{\nabla O}{|\nabla O|}\right) X'\mathrm{d}\mathbf{r} \tag{12}$$

From Equation 12 it follows that the minimization of Equation 11 with respect to O equals to solving:

$$\int_{\mathbf{r}} H(-\mathbf{r})\mathrm{d}\mathbf{r} - H(-\mathbf{r}) * \frac{Y(\mathbf{r})}{(H * O)(\mathbf{r})} - \lambda\mathrm{div}\left(\frac{\nabla O}{|\nabla O|}\right) = 0 \tag{13}$$

Rearranging Equation 13 and solving it in an iterative multiplicative manner yields the EMMLTV algorithm of O:

$$O_{k+1} = \frac{O_k}{1 - \lambda\mathrm{div}\left(\frac{\nabla O}{|\nabla O|}\right)}\left[H(-\mathbf{r}) * \frac{Y(\mathbf{r})}{(H * O)(\mathbf{r})}\right] \tag{14}$$

The matrix form of Equation 14 is given by:

$$O_{L,TV} = O_L. \times H_L^T(Y_L./H_LO_L)./(1 - \lambda TV(O_L)) \tag{15}$$

where the TV term stands for the discrete calculation of $\lambda \text{div}\left(\frac{\nabla O_L}{|\nabla O_L|}\right)$. The discrete computational implementation thereof is given by [43]. Note that this algorithm for computing O_L and H_L does not contain the acceleration component ω and acceleration parameter α that Equation 2.5 contains. Those parameters were added for increased convergence speed and algorithm stability.